UNIVERSITY OF MILAN

DEPARTEMENT OF VETERINARY MEDICINE

PhD course in
Veterinary and Animal Science

Class XXXII

TUMOR MICROENVIRONMENT IN EXPERIMENTAL PRECLINICAL MOUSE MODELS OF HUMAN CANCER: MORPHOLOGICAL APPROACH

PhD Candidate
Dr. Lucia MINOLI
Matricola n° R11650

Tutor: Prof. Eugenio Scanziani

PhD Course Coordinator: Prof. Valeria Grieco

ACADEMIC YEAR 2018/2019

I

Index

Abstract

One of the recent advancements in oncological research has been the recognition of the tumor microenvironment (TME) as a relevant participant during all stages of the evolution of a neoplastic process. Indeed, over the past decades, tumors have been considered through a changing perspective: no longer as a growth of homogeneous neoplastic cells, but as an actual organ composed of different cell populations and structures: the parenchyma being the neoplastic population and the stroma, including the vascular network and infiltrating cells.

The tumor microenvironment has a dual role in tumor biology, both promoting and antagonizing tumor development, growth and local or distant invasiveness. According to its leading role in influencing tumor biology each component of the TME could be considered as a potential pharmacological target to be enhanced or antagonized, in order to influence tumor behavior.

Accordingly, the study of the TME could provide new insights in the tumor biology and offers numerous potential targets for the development of novel therapeutic strategies. In this context, morphological techniques represent useful tools for the investigation of the TME, allowing the evaluation of the spatial distribution of the different elements, and provide useful complementary information to clinical and other data obtained in experimental *in vivo* studies.

In this thesis, the three main classes of the TME components -tumor-associated vasculature, immune-inflammatory cells and tumor stroma- are illustrated in three different chapters and relevant experimental studies described. However, it should be considered that the various aspects of TME are not separate entities but are all involved in a dynamic system with complex structural and functional interactions.

Chapter 1 – Tumor associated vasculature

Tumor angiogenesis has been identified as a hallmark of cancer, due to its central role in supporting tumoral growth, providing nutrient supply, removing catabolites and enabling tumoral metastatic dissemination. Most of the solid tumors are characterized by an "angiogenetic switch" in which an imbalance between pro- and anti-angiogenic factors sustains a dysregulated angiogenetic process, leading to the formation of an altered vascular network composed of structurally and functionally abnormal blood vessels. Drugs targeting tumor vasculature has been extensively studied as a mean to interfere with tumoral growth as well as to promote the delivery and/or effect of co-administered compounds to the tumor.

In the first study of this chapter we demonstrated the therapeutic efficacy and the antiangiogenic effect of a novel compound developed by binding sunitinib (a well-known antiangiogenic drug) to a selective binder of $\alpha_V\beta_3$ integrin thus promoting its delivery to the target site (tumors expressing $\alpha_V\beta_3$ integrin).

The other studies of this chapter investigated the relation between tumor vasculature and tumor hypoxia. In particular this relation was investigated to uncover the potential mechanism underlying the synergistic effect of the administration of an antiangiogenic compound (cediranib) with a poly-ADP ribose polymerase (PARP) inhibitor (olaparib) in a panel of patient derived xenografts of ovarian carcinoma.

Chapter 2 – Tumor immune microenvironment

In most cancers, both innate and acquired immunity have a driving role during all stages of tumor development and progression. Depending on the cell population and/or molecular stimuli received, they can act in dual way, antagonizing or promoting tumor growth.

Three selected studies were described in chapter 2 and investigated:

1. The role of NK cells in hindering metastasis engraftment in a metastatic model of synovial sarcoma. After the combined administration of an heparanase-inhibitor with a tyrosine kinase inhibitor a significant reduction of lung metastases was observed and immunohistochemical analyses demonstrated the role of NK cells in this phenomenon.
2. The macrophage polarization status in a panel of xenotransplanted thyroid carcinoma tumors. The mononuclear-phagocyte populations infiltrating the tumors were evaluated by immunohistochemistry.
3. The role of inflammation in the development of colorectal cancer was evaluated in mice (wild type and EMILIN1-mutant), undergoing administration of AOM-SS (chemical carcinogenesis model). EMILIN1 mutant mice developed more numerous and more severe tumoral lesions compared to wild type, as well as increased inflammatory infiltrate was observed, unveiling a potential contribution of Emilin 1 in the pathogenesis of colorectal adenocarcinoma.

Chapter 3 – Tumor stroma

Tumor stroma represents not only the scaffold in which tumors growth, but also an intricate network of molecules and signals influencing tumor biology.

The first study of this chapter investigated stroma-derived circulating molecules as a potential tool for the early diagnosis of pancreatic ductal adenocarcinoma (PDAC). Selected molecules (MMP-7, TIMP-1 and Throbospondin-2) were tested in KC genetically engineered mice (modeling the early stages of PDAC development) and patient-derived xenografts (modeling tumor progression), by serum ELISA and by immunohistochemistry.

The second study evaluated the potential improvement in the biodistribution of chemotherapeutic drugs derived from the combined treatment with hyaluronidase. Tumor-bearing mice (ovarian carcinoma and pancreatic carcinoma models) were treated with chemotherapy alone (paclitaxel) or combined with hyaluronidase. Hyaluronidase treatment reduced the amount of stromal hyaluronic acid (as demonstrated by Alcian blue stain) and improved intratumor distribution of paclitaxel (as analyzed by mass spectrometry).

Preface

Particularly in western countries, cancer represents one of the leading causes of death, being the 1st or 2nd cause of premature mortality in 91 out of 172 countries worldwide (fig. 1). Geographical distribution of the overall cancer incidence and mortality depends on several risk factors, including socioeconomic development. However, cancer epidemiology is in continuous evolution reflecting the modification of risk factors, important lifestyle changes in several regions but also prevention campaigns and new therapies which interfere with both incidence and mortality rates. Prevention and treatment represent two essential and not mutually exclusive strategies to control cancer and have partially improved cancer control over the last decades.
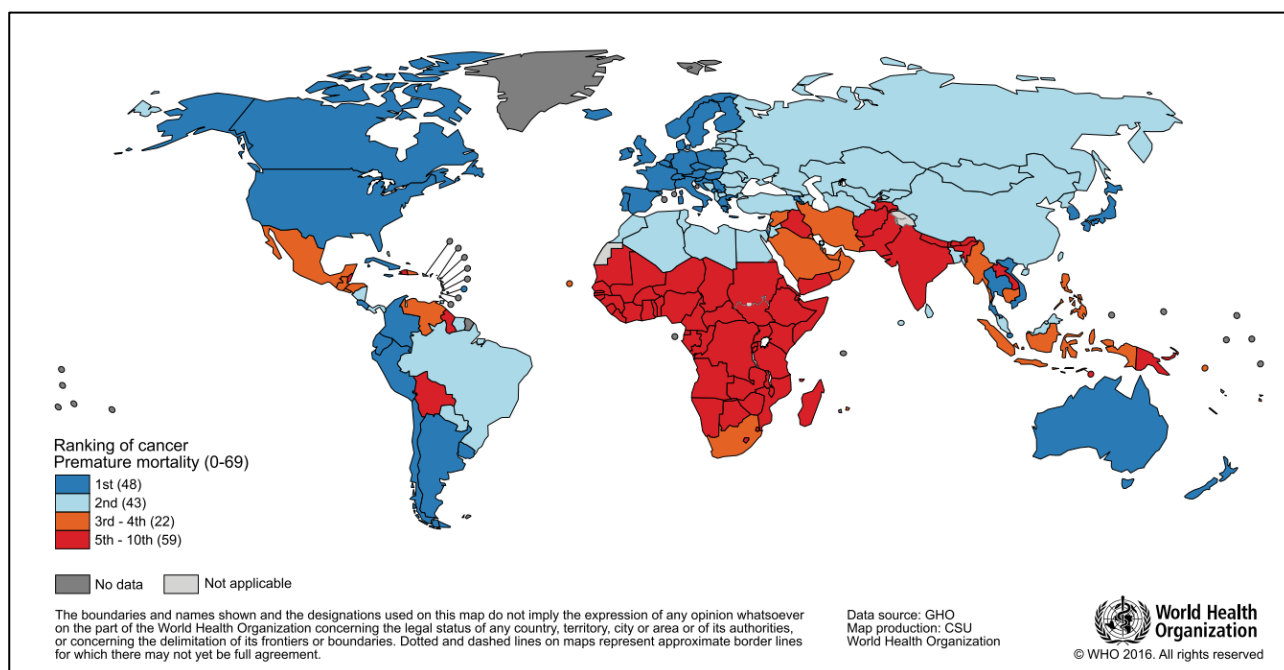
FIGURE 1 - Global map presenting the national ranking of cancer as a cause of death at ages below 70 years in 2015. Image source: WHO – Global cancer statistics [1].

Biomedical research at all levels, from basic and translational studies up to clinical trials, has contributed and continues to contribute to deepen our knowledge of tumor biology and to the discovery of novel diagnostic and therapeutic tools, ultimately improving patients' health.

One of the recent advancements in oncological research has been the recognition of the tumor microenvironment (TME) as a relevant participant during all stages of the evolution of a neoplastic disease. Indeed, over the past decades, tumors have been considered through a changing perspective: no longer as a growth of homogeneous neoplastic cells, but as an actual organ composed of different cell populations and structures: the parenchyma being the neoplastic population and the stroma, including the vascular network and infiltrating cells.

The tumor microenvironment has a dual role in tumor biology, both promoting and antagonizing tumor development, growth and local or distant invasiveness. According to its leading role in influencing tumor biology each component of the TME could be considered as a potential pharmacological target to be enhanced or antagonized, in order to influence tumor behavior.

Accordingly, the study of the TME could provide new insights in the tumor biology and offers numerous potential targets for the development of novel therapeutic strategies. In this context,

morphological techniques represent useful tools for the investigation of the TME, allowing the evaluation of the spatial distribution of the different elements, and provide useful complementary information to clinical and other data obtained in experimental *in vivo* studies.

In this thesis, the three main categories of the TME components -tumor-associated vasculature, immune-inflammatory cells and tumor stroma- are illustrated in three different chapters and relevant experimental studies described. However, it should be considered that the various aspects of TME are not separate entities but are all involved in a dynamic system with complex structural and functional interactions.

All the experiments presented hereafter were performed on mouse models of human cancer. In this regard, different types of models were used, and in particular:

- Patient-derived xenografts (PDXs) engrafted either subcutaneously or in orthotopic location in immunocompromised mice. All the PDXs used in the following studies were obtained from the biobank of the Oncology Department, Istituto Mario Negri (Milan) and were in-house developed PDXs.
- Tumoral cell lines of human origin engrafted either subcutaneously or in orthotopic location in immunocompromised mice.
- Chemically induced models (i.e. AOM-DSS colon carcinogenesis model).
- Genetically engineered mouse models (i.e. KC mouse model of pancreatic intraepithelial neoplasia).

All the studies presented hereafter were performed on mouse models of human diseases. *In vivo* experiments were performed according to the current national laws on laboratory animal welfare (D. Lgs. 26/2014) and to the animal welfare guidelines for oncological research [2].

Chapter 1 - Tumor Associated Vasculature

1.1 Introduction

1.1.1 Tumor angiogenesis

Angiogenesis is defined as the formation of new blood vessels in adult individuals; it arises both in physiological settings (e.g. wound healing) and pathological processes, such as solid tumors.

In adult individuals, in physiological conditions, endothelial cells are in a quiescent state, fostered by pericyte coverage which supports their metabolism and suppresses proliferation. Neoangiogenesis is triggered by specific stimuli, such as angiogenic factors released by hypoxic cells. Thus, pericytes detach from the vessel wall via a proteolytic mechanism mediated by matrix metalloproteinases (MMPs), inducing sprouting of new blood vessels and promoting the extension of the vascular network in order to sustain tissue metabolism [3].

Tumor angiogenesis has been identified as a hallmark of cancer [4], due to its central role in supporting tumoral growth, providing nutrient supply and removing catabolites [5]. Besides, it plays a key role in enabling and promoting tumoral metastatic dissemination [4].

Most of the solid tumors are characterized by an "angiogenetic switch" in which an imbalance between pro- and anti-angiogenic factors sustains a dysregulated angiogenetic process. The main angiogenic inducer is the vascular endothelial growth factor A (VEGF-A); when bound to one of its receptors (represented by three different tyrosine kinase receptors, VEGFR-1 - 3), VEGF-A promotes blood vessels proliferation and permeability [3].

Different tumor types (e.g. ovarian cancer) overexpress VEGF, which by acting through a paracrine mechanism, promotes angiogenesis and sustains tumor metabolism. Furthermore, latent forms of VEGF can be sequestered in the extracellular matrix (ECM) and then released and activated upon the action of ECM-degrading enzymes (e.g. MMP-9).

Morphological studies demonstrated that generally tumoral vessels are structurally and functionally abnormal [6]. The most common abnormal features of tumor blood vessels described in the literature are as follows:

- Disorganized vascular network, characterized by high number of intersecting blood vessels, with irregular branching pattern and without a clear dividing hierarchy (i.e. arterioles, capillaries, venules), with several blind-end branches (fig. 1.1) [7,8].
- Endothelial cells are irregularly shaped, presenting multiple cytoplasmic processes, and occasionally overlap with other endothelial cells, producing a rough luminal surface. Moreover, the presence of high number of large and irregularly spaced intercellular openings in some tumors are responsible for blood vessels leakiness [7].
- Pericytes are irregularly distributed along the vessel wall, resulting in an overall reduced pericyte coverage of the vessel. These are loosely associated with the endothelium and have cytoplasmic processes that penetrate deep into the surrounding tumor parenchyma [8]. Furthermore, pericytes regularly accompany and precede sprouts of branching and growing blood vessels, probably driving the expansion of the vascular network [8].
- Basement membrane of irregular thickness and with multifocal defects or which is characterized by multiple layers and is loosely associated with endothelium and pericytes. All these features are reminiscents of degenerating and regenerating blood vessels [9].

It is important to underline that neoangiogenesis is not the only way in which blood supply is provided to the tumor. Vasculogenic mimicry was firstly described in uveal melanoma in 1999 by Maniotis et al. (1999) [10] and consists in the formation of blood-filled channels lined by tumoral cells and basement membrane, providing nutrients to the tumor [11]. Vasculogenic mimicry was thereafter demonstrated in several tumor types, and in some of them correlated with poor prognosis (glioma, colorectal adenocarcinoma, non-small cell lung cancer,…) [11].
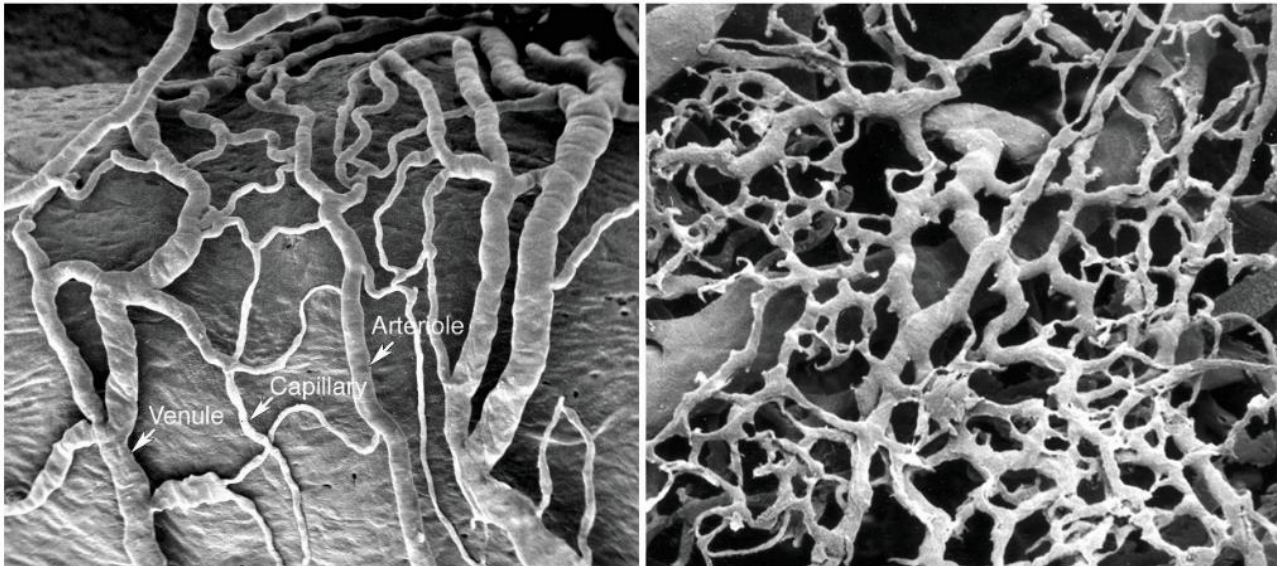
FIGURE 1.1 – Scanning electron microscopy of normal blood vessels (left) characterized by organized vascular network and neoangiogenic tumoral blood vessels (right) showing disorganized vasculature with unsystematic branching hierarchy. Image source: McDonald & Choyke, 2003 [12].

1.1.2 Tumor hypoxia

The above-described altered vascular network is responsible for impaired blood flow within the tumor, leading to the formation of hypoxic areas and intratumoral acidosis [6,13]. Hypoxic regions within tumoral masses do not hinder tumor growth, but, on the contrary, select more aggressive cellular clones, able to adapt to adverse environmental conditions and to decrease the effectiveness of antitumor immunity [14,15]. Accordingly, extensive hypoxia is associated with poor prognosis in several tumor types [16]. Moreover, intratumor hypoxia is also responsible for tumor resistance to different conventional anti-tumor treatments such as radiotherapy [17] and microtubule-stabilizing drugs (i.e. taxanes) [18] as well as novel antitumor approaches (i.e. immunotherapy).

Two types of hypoxia have been recognized in tumors: the diffusion-limited hypoxia (or chronic hypoxia) and the perfusion-limited hypoxia (or acute hypoxia) [19]. The first one depends on the distance between the vessel and the tissue area and is characterized by reduced oxygenation of cells at a greater distance from a tumor vessel [19]. On the other hand, perfusion-limited hypoxia is related to fluctuations in blood supply or blood oxygenation, leading to intermittent hypoxia. Reported causes for the fluctuation in blood flow are temporary occlusion of vessels by fibrin thrombi or tumoral emboli, arterial vasomotion or vascular remodeling [20].

The master regulator of tumor cells under hypoxic conditions is the complex of hypoxia inducible factors (HIFs). HIFs are composed of an oxygen-dependent α subunit and an oxygen-independent β subunit. When oxygen concentration is <6%, the α subunit is translocated to the nucleus, dimerizes with the β subunit and the resultant HIF-1 induces the transcription of different genes implicated in the regulation of angiogenesis, cell metabolism, anaerobic energy supply, pH balance and apoptosis [21]. Tumor cells are frequently subjected to a metabolic switch from aerobic

metabolism (i.e. oxidative phosphorylation) to an anaerobic one (i.e. anaerobic glycolysis) also at normal oxygen tension levels. This phenomenon is known as *Warburg effect* and is due to the stabilization of HIF1-α [21].

Persistent activation of HIF-1 induces various effects which promote tumor resistance and growth. The effects of tumor hypoxia on tumor cells and on the tumor microenvironment interact and are related with several of the hallmarks of cancer described by Hanahan and Weinberg (2011) [4]:

- *Sustaining proliferative signal.* In tumoral cells, cell proliferation is promoted and maintained by either mitogenic growth factors or by the constitutive activation of the downstream pathways. Hypoxia can induce cancer cells to express several growth factors (e.g. EGF, insulin, IGF-1, IGF-2, and PDGF), consequently promoting cell proliferation without being dependent on exogenous mitogenic signals [22].
- *Resisting cell death.* Although hypoxic conditions usually activate and promote apoptosis in normal cells, cancer cells frequently develop various mechanisms for escaping HIF-1-mediated apoptosis, such as activation of the PI3K/AKT pathway. Accordingly, a hypoxic microenvironment induces the selection of tumor cell clones resistant to hypoxia-induced apoptosis [22].
- *Inducing angiogenesis.* The activation of HIF-1 induces the transcription of several genes involved in the angiogenic process (e.g. VEGF), and hypoxia decreases the activity of antiangiogenic matricellular proteins (i.e. thrombospondin). Consequently, the protracted stimulus for angiogenesis leads to the expansion of the typically abnormal vascular network, perpetrating the vicious cycle [22].
- *Avoiding immune destruction and inducing tumor promoting inflammation.* It has been demonstrated that a hypoxic microenvironment suppresses antitumor immunity. Indeed, it promotes the polarization of macrophages into an M2 phenotype (protumoral macrophages), inhibits the activity cytotoxic $CD8^+$ T lymphocytes and hinder the antigen presentation activity of dendritic cells [22,23].
- *Activating invasion and metastasis.* Several studies have shown a correlation between tumor hypoxia and metastatic dissemination. Although the precise mechanisms for this event are still unknown, it probably involves the epithelial to mesenchymal transition, likely driven by HIF overexpression in hypoxic cells [22].
- *Genome instability and mutation.* Genomic instability and mutations are determined by several mechanisms including suppression of DNA mismatch repair genes, homologous recombination genes, increased chromosomal rearrangement and gene amplification [22].

1.1.3 Antiangiogenic therapy
Considering the above-described features, therapeutic strategies targeting tumor associated vasculature had been developed in the last decades. Initially, the rationale underlying antiangiogenic therapy was to reduce tissue perfusion and consequently to "starve" the tumor, slowing its growth and promoting cancer cell death [24].

However, the evidence that the administration of antiangiogenic drugs in monotherapy provided only modest therapeutic benefit, led to a change of perspective. More recently, the administration of antiangiogenic compounds is thought to induce normalization of tumor vessels, improving blood perfusion, decreasing interstitial pressure and supporting drug delivery to the tumor [25]. Indeed, improved efficacy has been obtained by combining antiangiogenic compounds with traditional chemotherapy. Moreover, better perfusion results in lower hypoxia with important consequences on tumor behavior as described above [14,15].

Bevacizumab was the first FDA-approved antiangiogenic agent for cancer treatment. It was initially approved in 2004 for colorectal adenocarcinoma and in subsequent years for ovarian carcinoma, breast cancer and non-small cell lung cancer. Bevacizumab is a humanized monoclonal antibody against VEGF-A. It inhibits VEGF-A binding to its receptor and consequently blocks the activation of VEGF pathway. Most of the other antiangiogenic compounds (tab. 1.1) currently approved in clinical practice are tyrosine kinase inhibitors (TKI), such as sunitinib, which antagonize, among other receptors, VEGFR.

TABLE 1.1 – List of FDA-approved antiangiogenic agents. Modified from: Al-Abd et al, 2017 [26].

Anti-angiogenic agent	Targeted pathway	Clinical indications
Bevacizumab	Humanized monoclonal anti-VEGF-A antibody	Several solid tumors (e.g. non-small cell lung carcinoma, renal carcinoma, colorectal carcinoma, ovarian carcinoma, breast carcinoma, cervical carcinoma, glioblastoma)
Ziv-aflibercept	Fusion protein directed against VEGF-A, VEGF-B, PIGF	Metastatic colorectal carcinoma in combination with 5-FU, irinotecan, leucovorin
Sorafenib	Multi-tyrosine kinase inhibitor	Hepatocellular carcinoma, renal cell carcinoma, thyroid carcinoma
Sunitinib	Multi-tyrosine kinase inhibitor	Hepatocellular carcinoma, renal cell carcinoma, thyroid carcinoma
Axitinib	Receptor tyrosine kinase inhibitor	Advanced renal cell carcinoma
Nintedanib	Receptor tyrosine kinase inhibitor	Idiopathic pulmonary fibrosis
Regorafenib	Receptor tyrosine kinase inhibitor	Metastatic colorectal carcinoma, GIST, hepatocellular carcinoma
Pazobanib	Receptor tyrosine kinase inhibitor	Advanced renal cell carcinoma, advanced soft tissue sarcoma
Cebozantinib	Receptor tyrosine kinase inhibitor	Metastatic medullary thyroid carcinoma
Vandetanib	Receptor tyrosine kinase inhibitor	Medullary thyroid carcinoma
Thalidomide	Inhibitor of Akt phosphorylation	Multiple myeloma in combination with dexamethasone

1.2 Experimental Studies

STUDY I - Quantification of tumor-associated vasculature in a mouse model of human ovarian carcinoma

The present study was conducted in collaboration with the Molecular Pharmacology Unit, Fondazione IRCCS Istituto Nazionale dei Tumori (Milan, Italy). For further details refer to appendix I, publication #1.

Ovarian carcinoma is the most lethal gynecological malignancy and it is characterized by high resistance to different therapeutic treatments [27].

Thanks to the biological relevance of tumor angiogenesis and its possible antagonization by means of antiangiogenic compounds, the evaluation of tumor-associated vasculature has gained importance either for prognostication in clinical practice, as well as to evaluate treatment effectiveness in preclinical models. *Ex vivo* morphological quantification of tumor-associated vasculature is commonly performed on histological samples stained by immunohistochemistry (IHC) for an endothelial marker (e.g. CD31). Usually, together with a morphological evaluation of blood vessels, two different quantitative parameters could be assessed: microvessel density (MVD) and vessel area (VA). Microvessel density refers to the number of vessels per unit of area (1 mm^2). It is the most used parameter also in human surgical pathology and is performed by counting the number of every immunoreactive endothelial cells or cluster of cells, clearly separated from adjacent vessels [28]. Vessel area is the measure (in μm^2) of the IHC- labeled region per unit of area. Vessel area is commonly expressed as a percentage (area fraction).

In the present experiment, both parameters were measured in order to evaluate the antiangiogenic activity of a novel therapeutic compound (named compound 3) compared to a traditional antiangiogenic drug (sunitinib) and untreated (control) mice. Since some integrins are upregulated in cancer, including ovarian carcinoma, they represent a potential target for drug delivery. In the present study, in order to improve the delivery to the tumor of the antiangiogenic drug sunitinib, a novel compound obtained by combining a molecule of sunitinib with a selective binder for the extracellular domain of $\alpha_V\beta_3$ integrin, was produced (compound 3).

Materials and methods

In vivo experiment. 21 female athymic CD-1 nude mice, 8–10 weeks-old, were subcutaneously injected with the IGROV-1Pt1 cell line and randomized in the 3 treatment groups reported in table 1.2. IGROV-1Pt cell line is the cisplatin-resistant variant of the widely used human-derived IGROV-1 parental cell line of ovarian carcinoma. Monitoring of tumor growth and determination of tumor volume inhibition (TVI) was done as reported in appendix II.

TABLE 1.2 – Experimental groups.

Group	Treatment	n° of mice
Control	Vehicle	7
Compd 3	Antiangiogenic compound under test, obtained by linking a molecule of sunitinib to a selective binder for $\alpha_V\beta_3$ integrin	7
Sunitinib	Antiangiogenic molecule	7

Histopathology. Subcutaneous tumors were collected, formalin-fixed and paraffin-embedded. From each sample, 4 um serial sections were stained with Hematoxylin and Eosin and by

immunohistochemistry with CD31 primary antibody (see appendix III and IV). Microvessel density (MVD) and the percentage of CD31-positive area (vessel area) were assessed in 3 randomly selected microscopic fields at 200x magnification, within the bulk of the tumor and avoiding areas of necrosis (see appendix VII).

Histopathological evaluation was performed blinded (i.e. without knowledge of the treatment group).

Statistics. Normal distribution of data was confirmed with Kolmogorov-Smirnov test. Differences among groups were analyzed with one-way ANOVA followed by Tukey's post-hoc test. Differences were considered significant when p<0.05.

Results

The antitumor activity of the 2 drugs was evaluated by monitoring tumor growth (fig. 1.2 A). Sunitinib strongly inhibited tumor growth with a TVI of 80% at day 20 post injection. Compound 3 demonstrated a TVI of 60% at day 20 post injection. Both drugs (sunitinib and compd3) significantly reduced tumor associated vasculature compared to untreated controls, both analyzing the number of blood vessels (MVD) and the CD31+ area (vessel area) (fig. 1.2 B, C and D).
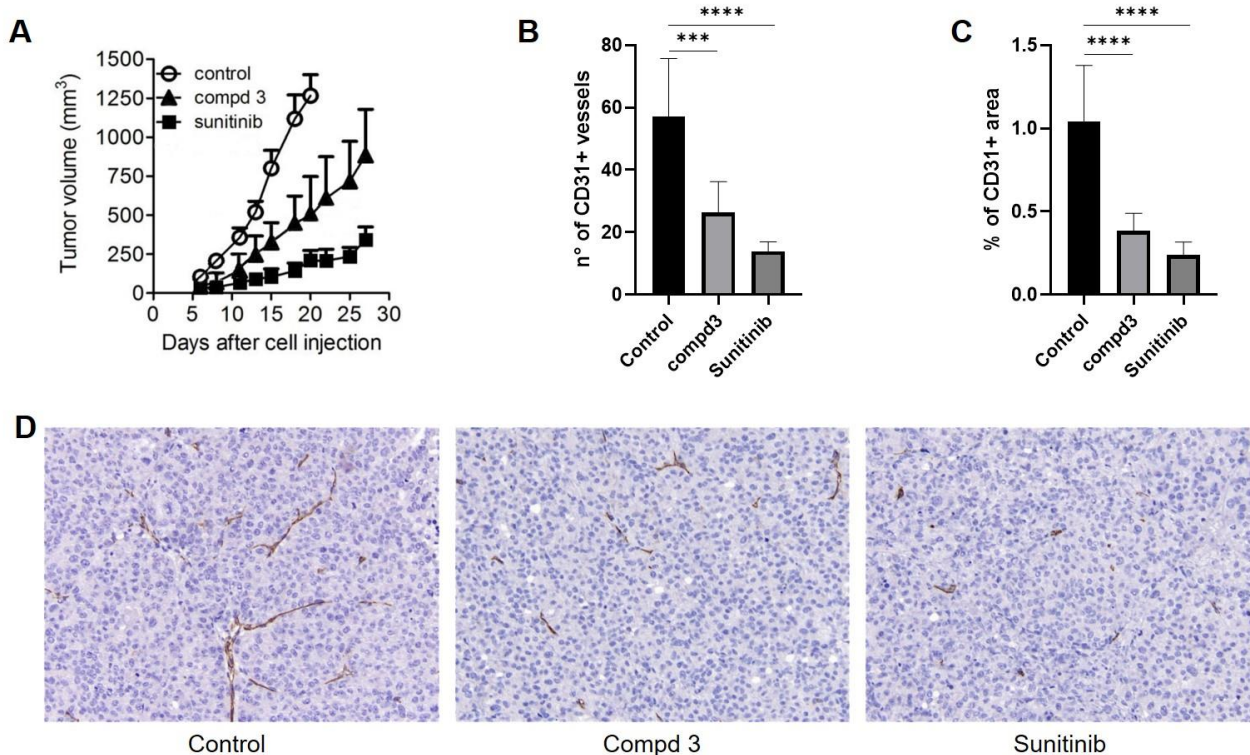
FIGURE 1.2 – A) Growth curves showing antitumor activity of compd 3 and sunitinib. B) both sunitinib and compd 3 efficiently reduced microvessel density and C) vessel area. D) Representative images of CD31 immunohistochemistry, 200x magnification. Modified from Sartori et al., 2019[29].

Conclusions

The present experiment demonstrated good efficacy of compound 3 in inhibiting tumoral growth. Reduced efficacy is observed if compared to classically administered sunitinib, but it should be considered that in compd3-treated group the total amount of administered sunitinib (included in the compound) was approximately 9 folds lower than in sunitinib group. Accordingly, both compd 3 and

sunitinib determined a strong and comparable reduction in vascularization, both when evaluated by VA and MVD.

The overall comparable efficacy of compd 3 and sunitinib, is likely due to a better biodistribution of the active compound (sunitinib), when delivered through compd 3, compared to the administration of sunitinib itself. The possibility to obtain comparable effects (particularly antiangiogenic effects) through the administration of a significantly lower dose of sunitinib, represents a great opportunity to improve the safety of the drug and the ensuing possibility to reduce side effects.

STUDY II - Immunohistochemical evaluation of tumor hypoxia

Evaluation of tumor hypoxia can be performed with several distinct techniques both *in vivo* and *ex vivo*. The evaluation of tissue hypoxia in histological sections can be performed by immunohistochemical evaluation of endogenous hypoxia-related markers (e.g. HIF-1, GLUT1 or CA9) or exogenously administered compounds, which bind to hypoxic cells (e.g. pimonidazole) [30].

Pimonidazole is part of the 2-nitroreductase molecules. After exogenous administration of the compound, at cellular conditions of $pO_2 < 10$ mmHg pimonidazole is reduced by cellular nitroreductases, and permanently binds to cellular proteins. The rate of binding could be different depending on tissue activity, but the absence of active enzymes in necrotic cells impedes the binding of pimonidazole to necrotic cells [30].

CA9 is an endogenous enzyme involved in the regulation of intracellular pH and cellular respiration. Its expression is regulated by HIF-1. However, it needs to be remarked that several factors other than hypoxia, could up or down regulate endogenous enzymes involved in the response to hypoxic stimuli [30]. Accordingly, the up regulation of CA9 is not necessarily related to low oxygen tensions but could be influenced by microenvironmental factors (such as glucose deficiency or pH alteration) or metabolic switch of tumoral cells (i.e. Warburg effect).

In the next two experiments, the technical set up of different immunohistochemical staining techniques for the evaluation of tissue hypoxia in histological samples are described.

EXPERIMENT I - IHC SET UP OF PIMONIDAZOLE

Since previous reports reported substantial differences in pimonidazole staining when evaluated on frozen vs formalin fixed paraffin embedded (FFPE) sections [31], indicating lower areas positively stained in FFPE compared to the frozen samples, the setup of the anti-pimonidazole primary antibody was performed both on FFPE and frozen samples and results compared.

Materials and methods

Two different tumoral models (ovarian carcinoma patient-derived xenografts, models "A" and "B"), subcutaneously engrafted into nude mice, were collected according to the protocol reported below.

A single dose of pimonidazole hydrochloride (Hypoxyprobe) was intravenously administrated 30 minutes before humane euthanasia of mice. *Post-mortem*, the tumor was isolated from surrounding tissues, and two adjacent, paracentral, 3 mm thick slices, were cut from each tumor xenograft. One was formalin fixed for 24 hours, processed for paraffin embedding (FFPE) and cut in 4 um thick sections at the microtome. The other slice was snap frozen, embedded in OCT and cut at the cryostat. An additional sample collected from an untreated mouse was FFPE and used as negative control. Samples were stained by immunohistochemistry with pimonidazole primary antibody (appendix III).

For FFPE samples the applied immunohistochemical protocol is reported in appendix IV. For frozen sections, two different protocols were used:

1. One section from each sample was fixed for 10 minutes in cold acetone (-20°C), and then immunohistochemically stained as described in the enclosed protocol (appendix IV), starting from the step "endogenous peroxidase blocking".
2. Another section from each sample was fixed in 10% neutral buffered formalin for 10 minutes at room temperature, washed in deionized water and immunohistochemically

stained as described in the enclosed protocol (appendix IV), starting from the step "epitope retrieval".

Additional negative controls for each IHC protocol tested, were obtained by substituting the primary antibody with 10% normal goat serum.

Results

All the sections stained with the three different protocols described above, demonstrated similar staining pattern. In particular, in tumoral model "A" (fig. 1.3), characterized by a cysto-papillary morphology, a progressive increase in the intensity of staining was observed from the base to the apex of the papillae. The result obtained reproduced the expected staining pattern: the presence of vessels in the stromal area of the tumor (asterisk), allows a better perfusion of the basal areas of the tumor compared to the apex of the papillae.

Tumoral model "B" was characterized by a solid pattern of growth, admixed with wide necrotic areas. In both FFPE and frozen samples a patchy positivity was observed throughout the sample, with a more intense staining in areas adjacent to necrosis, without staining necrotic areas.

No background staining was detected in the sample collected from the untreated mouse.
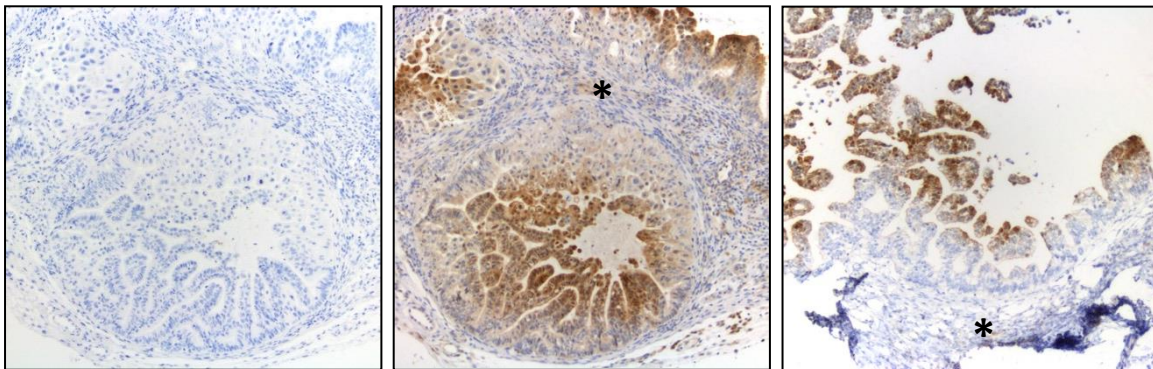
FIGURE 1.3 – Example of immunohistochemistry staining for pimonidazole, from tumoral model "A". Negative control (left); FFPE sample (middle); frozen sample (right). * = tumoral stroma.

Conclusions

Immunohistochemical staining with anti-pimonidazole primary antibody demonstrated a similar pattern of staining in both FFPE and frozen sections. Accordingly, for the subsequent experiments, the FFPE procedure was used because of a better preservation of tissutal features and morphological detail and because all the other antibodies applied were already set up on FFPE samples.

EXPERIMENT II - PIMONIDAZOLE VS CA9 IMMUNOHISTOCHEMISTRY
Experiment II was performed in order to compare the staining pattern obtained by pimonidazole and CA9 immunohistochemistry.

Materials and methods

FFPE samples were obtained from control mice from different experiments of subcutaneous xenotransplantation of tumors, in order to compare different tumoral models characterized by different morphological features and architectural arrangement. In particular, two ovarian

carcinoma patient-derived xenografts (PDX1 and PDX2) and two mammary carcinoma cell lines (MB231 and 0771-luc), grown subcutaneously in nude mice, were evaluated. All tumoral models used in the present study were of human origin.

Two 4 μm serial sections from each sample were cut at the microtome and stained by immunohistochemistry with anti-pimonidazole and anti-CA9 primary antibodies (see appendix III and IV), and results compared.

Results

Overall, the staining pattern of the two markers was similar and tissutal distribution of hypoxic areas comparable when evaluated with pimonidazole and CA9. Pimonidazole showed diffuse nuclear and cytoplasmic staining of positive cells, while in CA9 stained sections the positivity was membranous.

Tumoral models characterized by a solid pattern of growth were frequently characterized by a wide central area of lytic necrosis often underlying a cutaneous ulcer. This finding was particularly present in mammary carcinoma models even when tumoral masses were collected at early time points (approximately 300 mg of tumor weight). In these models, a rim of hypoxic cells surrounded the central necrotic area (fig. 1.4) and in the surrounding parenchyma, pimonidazole and CA9 staining were variably distributed. For example, in one model of ovarian carcinoma (PDX1) organized in solid areas growing around an ectatic central blood vessel, progressive increase of intensity of the staining was observed from the perivascular central areas to the outermost areas of the tumor.

In another ovarian carcinoma model (PDX2), characterized by a cysto-papillary architecture a progressive increase in the intensity of the staining was observed from the base to the apex of the papillae (fig. 1.5). In one mammary carcinoma cell line (0771-luc cell line) CA9 was expressed by rare tumoral cells, not mirroring pimonidazole staining distribution.
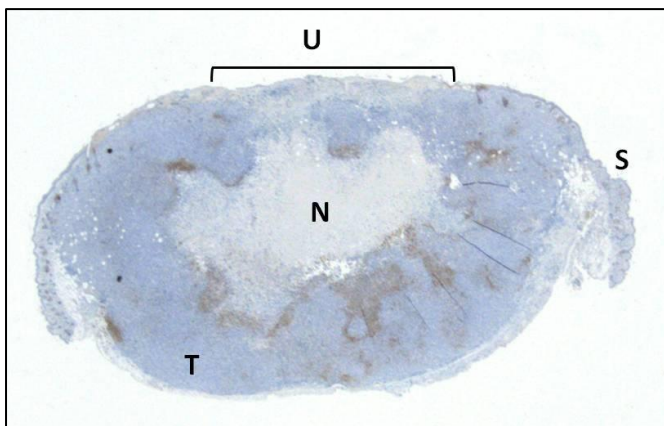
FIGURE 1.4 – Representative distribution of hypoxic areas in a subcutaneous xenograft. Mammary carcinoma MB231 cell line, IHC for pimonidazole, 2.5x magnification. T=tumor; N=necrosis; S=skin; U=ulcer
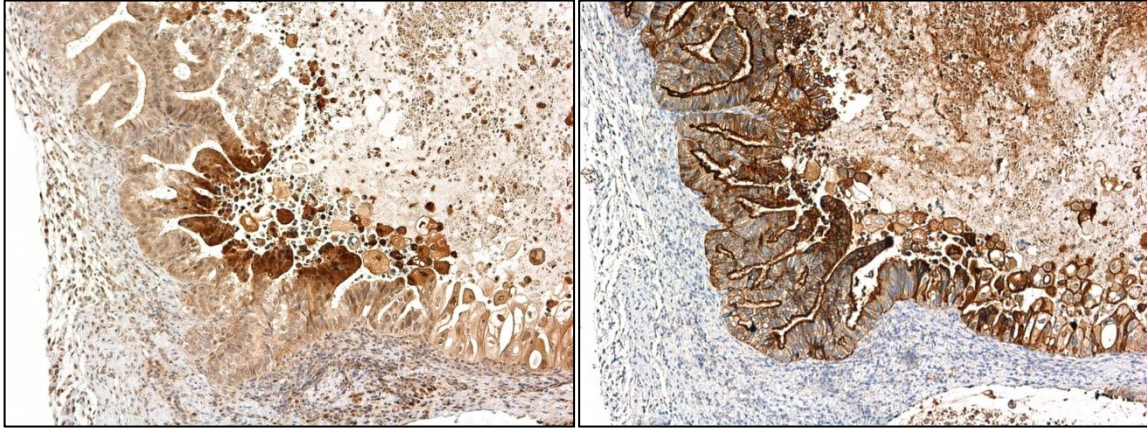
FIGURE 1.5 – Human ovarian carcinoma PDX. Immunohistochemistry for pimonidazole (left) and CA9 (right).

Conclusions

In the present experiment distribution of tumor hypoxia was evaluated with two different immunohistochemical markers. Both pimonidazole and CA9 markers demonstrated good quality and a similar staining distribution.

In one model, only rare tumoral cells expressed CA9, confirming that the expression of endogenous hypoxia markers is dependent also on other factors (cell line, tumor metabolism,…). Accordingly, in study III -when possible- pimonidazole stain was preferred for the evaluation of tumor hypoxia.

STUDY III - Tumor associated vasculature and tumor hypoxia in experimental models of human ovarian cancer treated with a combination of antiangiogenic and PARP-inhibitor agents

The present study was conducted in collaboration with Laboratory of Cancer Metastasis Therapeutics, Istituto di Ricerche Farmacologiche Mario Negri (Milan, Italy).

Human ovarian carcinoma is a heterogeneous disease characterized by different histological subtypes which differ in histogenesis, molecular features and, most of all, clinical behavior [32,33]. Despite that this heterogeneity is widely recognized, the therapeutic approach for ovarian carcinoma is still univocal and mainly represented by debulking surgery associated with platinum-based chemotherapy. In the last years, large attention was given to target therapies as new therapeutic strategies to improve patients' outcome. In the present preclinical study, we investigated the combination of two different target compounds, namely a PARP-inhibitor and an antiangiogenic compound.

Poly (ADP-ribose) polymerase (PARP) is a family of enzymes involved in single strand DNA repair. The administration of PARP-inhibitors molecules (PARPi) leads to a DNA damage that normal cells could efficiently repair by homologous recombination mechanisms [34]. On the contrary, neoplastic cells with impaired homologous recombination mechanisms, such as those carrying a mutation on BRCA1 and/or BRCA2 genes, undergo synthetic lethality. High grade serous ovarian carcinoma patients with a BRCA1/2 mutation (BRCAness), obtained a benefit from PARPi treatment [35]. Although the mechanism is not completely understood, previous studies have demonstrated partial effectiveness of the treatment with PARPi also in non-mutated patients (not-BRCAness) [36].

The combination of PARPi and antiangiogenic therapy could be a valuable therapeutic strategy, as the removal of the vascular support to the tumor could lead to a genetic instability, thus sensitizing neoplastic cells to PARPi activity. In the present study we tested the efficacy of the combination of olaparib and cediranib on a panel of both BRCAness and not-BRCAness ovarian cancer patient-derived xenografts. Olaparib is a PARPi approved for the treatment of germline BRCA mutated patients who have received three or more previous lines of platinum-based chemotherapy. Cediranib is a novel antiangiogenic compound which activity is related to the inhibition of the VEGF receptor.

Material and methods

In vivo experiment. Five different ovarian carcinoma patient-derived xenografts (PDXs) were established subcutaneously (n=4 PDXs, numbered from 1 to 4) or orthotopically (intraperitoneal injection, n=1 PDX, number 5) in nude mice. The panel of the investigated PDXs comprised both BRCAness (n=3 PDXs, number 3-5) and not-BRCAness (n=2 PDXs, number 1 and 2) tumors.

For each PDX model, after tumor engraftment, mice were randomized into 4 groups of treatment (control, cediranib, olaparib and combination; n=7/8 mice for each group) and the treatments were administered according to a pre-established schedule, from day 0 (randomization), until day 28.

For subcutaneous models, on day 28, 3 mice/group underwent humane euthanasia and samples (i.e. subcutaneous xenograft) were collected for histopathological assessment of treatment-related parameter. Remaining mice from each group (n=4/5) were monitored until the established humane endpoint was reached [2] and tumor growth was monitored as reported in appendix II. For the

intraperitoneal model, any mouse was sacrificed at day 28 and histopathological analyses were performed on three randomly selected mice sacrificed at the end of the experiment.
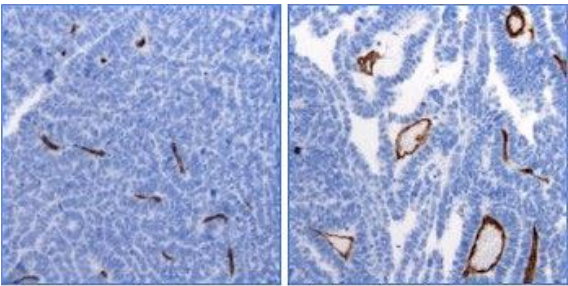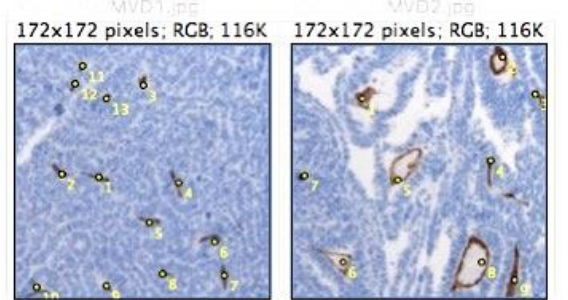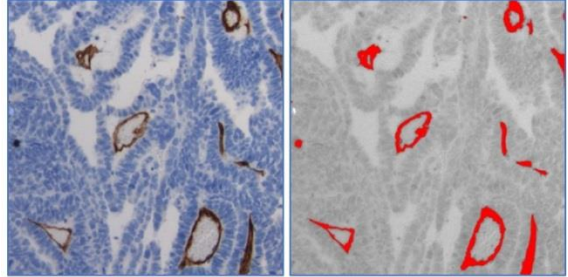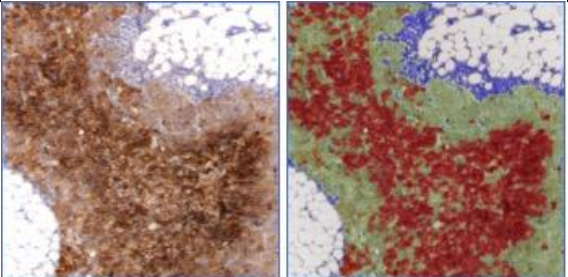
Histopathology. Histopathological analysis focused on the evaluation of:
- *Tumor associated vasculature*: a serial section from each sample were stained by immunohistochemistry with a rat monoclonal anti-CD31 primary antibody (see appendix III and IV). Three different parameters, listed in table 1.3, were therefore evaluated.
- *Tumor hypoxia*: a serial section from each sample were stained by immunohistochemistry with rabbit polyclonal anti-Pimonidazole or rabbit polyclonal anti-CA9 primary antibodies (see appendix III and IV). The immunopositive area was measured by digital image analysis (tab. 1.3).

Histopathological evaluation was performed blinded (i.e. without knowledge of the treatment group).

Statistics. Statistical differences among groups were evaluated by using the Kruskall-Wallis non-parametric test, followed by the post hoc Dunn's test. Differences were considered significant when $p < 0.05$.

TABLE 1.3 – Immunohistochemical parameters evaluated.

| Parameter	Method	Illustrative images of the method applied
Vessel morphology	Semiquantitative score to evaluate vascular abnormalities (e.g. blood vessels ectasia, tortuous development,…): 0=normal blood vessels; 1= <10% of blood vessels are abnormal. 2= 10-30% of blood vessels are abnormal. 3= >30% of blood vessels are abnormal.	Vessel morphology: score 0 (left) and 3 (right).
Microvessel density (MVD)	Manual count of the number of CD31+ vessels in 3 200x microscopic fields randomly selected across the tumor area (see appendix VII).	Manual count of the number of CD31+ vessels (MVD), with the aid of ImageJ software.
Vessel area (VA)	Measurement of the percentage of CD31+ area in 3 200x microscopic fields randomly selected across the tumor area, by using ImageJ analysis software (see appendix VII).	Digital image analysis of endothelial area. Original image (left) and elaborated image (right), with CD31+ vessels thresholded in red (VA).
Tumor hypoxia	Measurement of the percentage of Pimonidazole+ or CA9+ area in 2 50x microscopic fields randomly selected across the tumor area, by using Orbit image analysis software (see appendix VII).	Digital image analysis of hypoxic tumoral regions. Original image (left) and elaborated image (right), with adipose tissue (not elaborated), negative tissue (blue), lightly stained area (green) and intensely stained area (red).

Results

Subcutaneous models - "Clinical" response to treatments (tumoral growth). Overall, results obtained from the present experiment demonstrated high heterogeneity in the sensitivity of the tumors to the single treatments. Depending on the model, tumors showed complete response (PDX 3), partial response (PDX 2 and 4) or were completely resistant (PDX 1) to cediranib administration (fig. 1.6). Regarding the sensitivity to the PARPi, in general, growth of BRCAness tumors was effectively inhibited by the single treatment (fig. 16 C and D), while not-BRCAness tumors demonstrated a poor/null response (fig. 1.6 A and B). Interestingly, all the models, independently from the response to the single therapies, benefit from the combination treatment which was able to further reduce the tumoral growth compared to the single treatments.
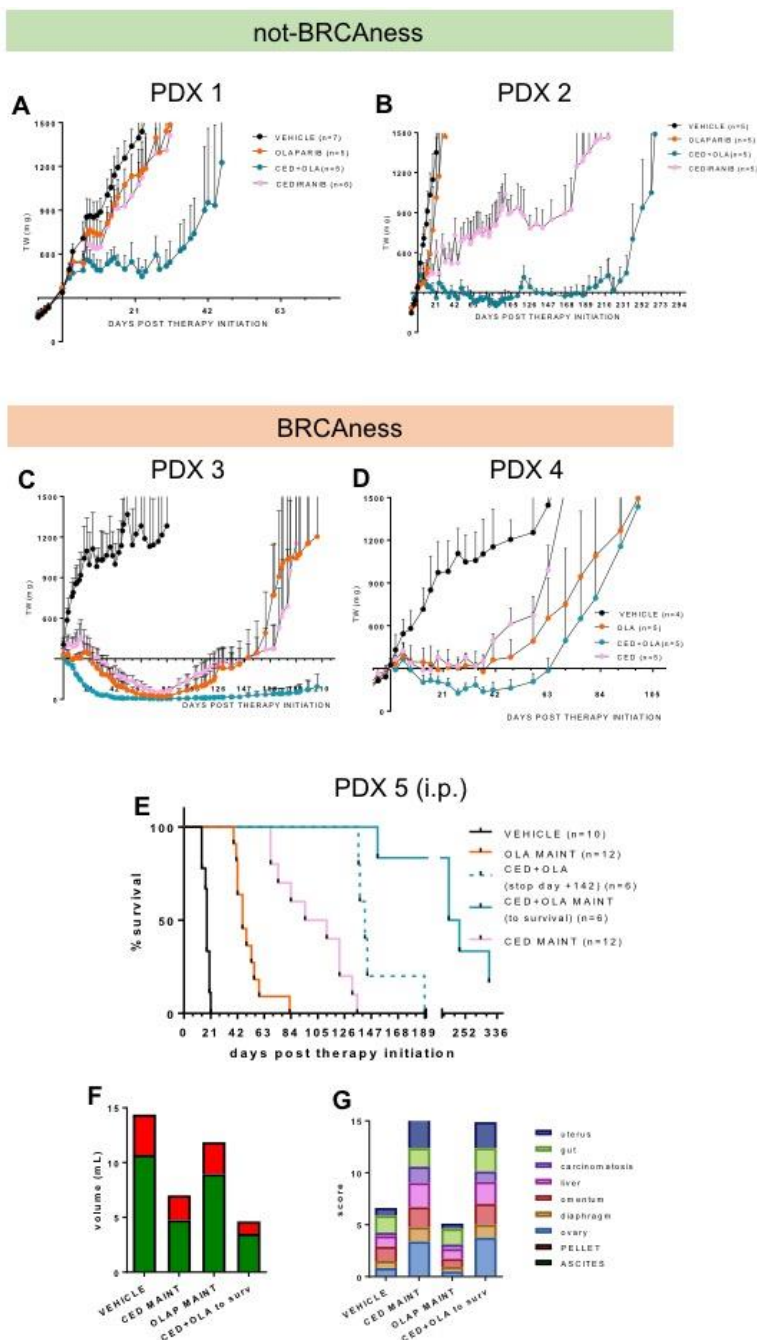
FIGURE 1.6 – Clinical response to treatments.
A, B, C, D) For each subcutaneous PDX tumor volumes were recorded from randomization until sacrifice. Groups of treatment are reported with different colors: black=control, pink=cediranib, orange=olaparib, green=combination.
E) PDX 5 was engrafted by intraperitoneal injection. Survival curves of the different groups are reported.
F) ascites volume collected at sacrifice from PDX 5 bearing mice. At sacrifice, cediranib-treated mice (second and fourth columns) had lower volume of ascites compared to the controls.
G) abdominal metastatic burden of PDX 5 bearing mice at sacrifice. At sacrifice, cediranib-treated mice (second and fourth columns) had higher metastatic burden compared to the controls.

Subcutaneous models - Antiangiogenic effect. Although the ability of cediranib to reduce tumor growth varied among the models, its effect on tumor associated vasculature was evident (with different magnitude) in all the models considered. Indeed, the antiangiogenic effect was demonstrated by the reduction in both MVD and EA upon the administration of cediranib as a single therapy as well as in the combination protocol (fig. 1.7 B and C). The only exception was the PDX 1 model (notoriously resistant to VEGFR inhibitors from previous experiments) where the cediranib-related decrease of vessels was minimal.

As antiangiogenic therapies are described to be able to "normalize" tumor vessels, a semiquantitative evaluation of vessel morphology was performed. In general, also in this case, the administration of cediranib alone or in combination, was effective in reducing vascular abnormalities (fig. 1.7 A).
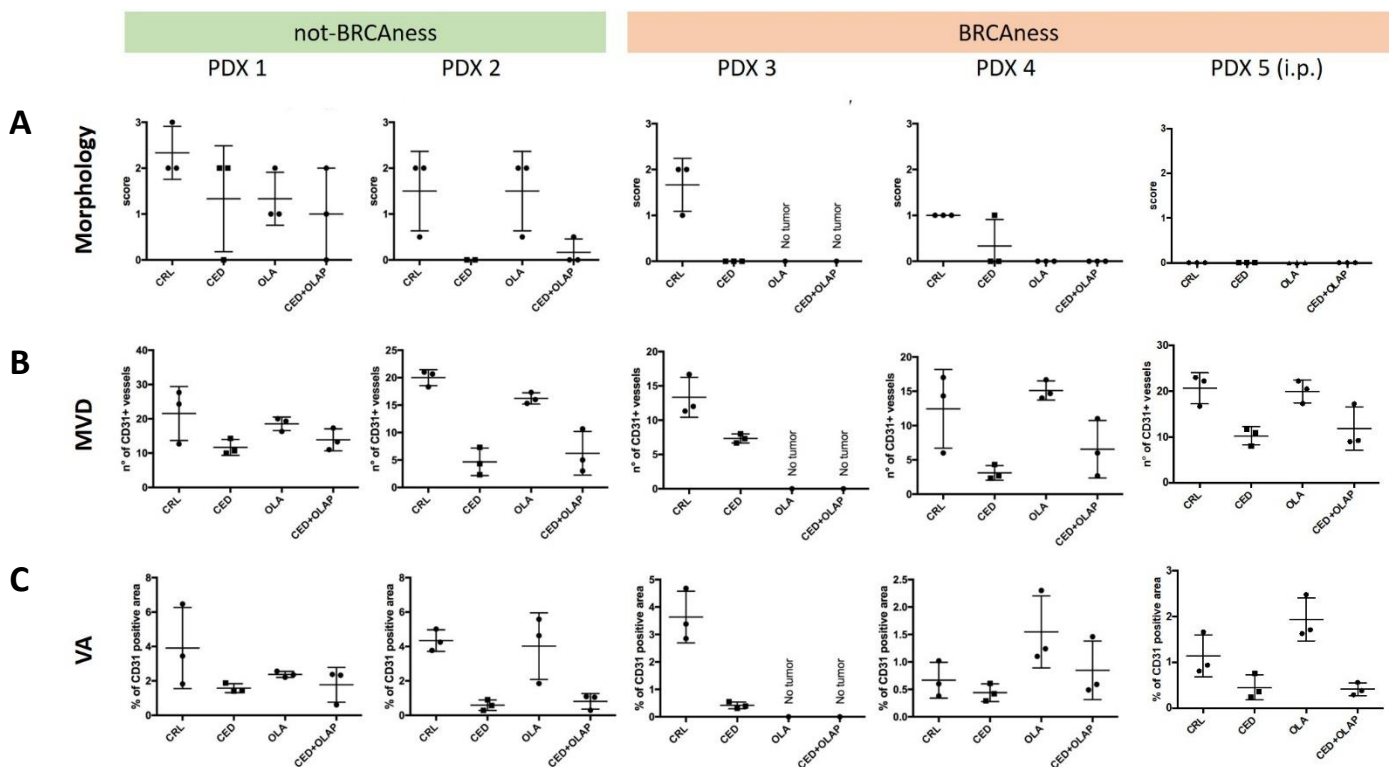
FIGURE 1.7 – Immunohistochemical analysis of tumor associated vasculature.
A) Morphological evaluation of blood vessels alterations (first line of graphs, "morphology"): in general, cediranib treatment (alone "CED" or in combination "CED+OLAP") reduced blood vessels alterations, compared to the controls ("CRL"). B) Microvessel density (second line of graphs, "MVD"): in general, cediranib treatment (alone "CED" or in combination "CED+OLAP") reduced MVD, compared to the controls ("CRL"). C) Endothelial area (third line of graphs, "VA"): in general, cediranib treatment (alone "CED" or in combination "CED+OLAP") reduced VA, compared to the controls ("CRL").
In PDX 3, no tumor masses were detected in samples from olaparib and combination groups, due to the high effectiveness of these treatments.

Subcutaneous models - Hypoxia. Tumor hypoxia was measured by pimonidazole or CA9 immunohistochemical stain. Overall, high heterogeneity was observed in tumor hypoxia in relation to treatments (fig. 1.8). This finding could be probably related to different sensitivity to the antiangiogenic treatment, to distinctive metabolic features of each tumor and partially attributable to tumor architecture. To give an example, opposite results were obtained in PDX 3 model (increase of hypoxia in cediranib group) and PDX 2 (decrease of hypoxia in cediranib and combination group). In PDX 3, neoplastic cells were arranged in solid areas, with central necrosis,

and dissected by ectatic blood vessels, forming vascular lacunae (fig. 1.9 A). This architecture resulted in a rim of hypoxic cells, surrounding necrotic areas, while the tumoral tissue surrounding blood vessels was negative to pimonidazole staining (fig. 1.9 C). In cediranib treated tumors, blood vessels lacunae were absent, few small vessels with virtual lumen were present in the tumoral stroma, necrotic areas were increased (fig. 1.9 B) and accordingly, diffuse and wider pimonidazole-positive tumoral areas were present (fig. 1.9 D).

On the contrary, PDX 2 was characterized by a cysto-papillary architecture supported by moderate to high amount of stroma in which blood vessels were mainly located (fig. 1.10 A). In this case, the tumoral tissue far from blood vessels (papillary structures projecting into the lumen) was hypoxic and therefore the tumor dimension had a stronger effect on hypoxia, resulting in lower hypoxic levels in smaller tumoral masses (cediranib and combination groups) (fig 1.10 D).
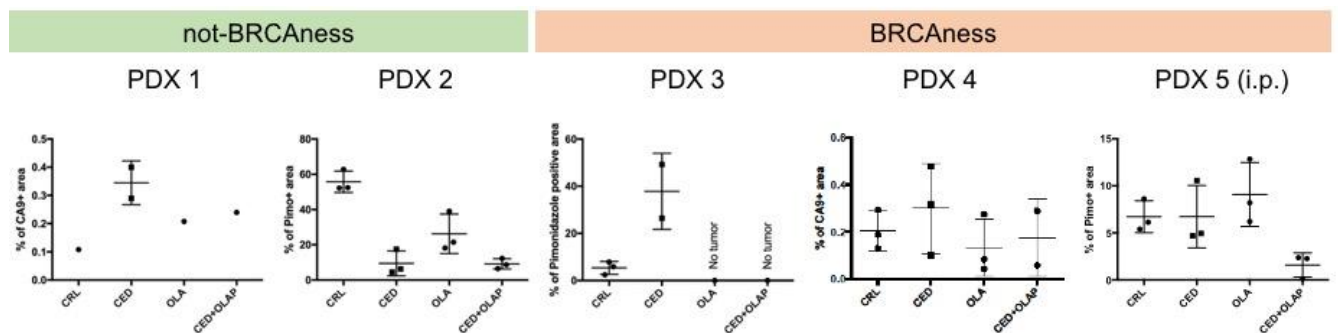
FIGURE 1.8 – **Immunohistochemical analysis of tumor hypoxia.** The two administrated compounds had variable effect on tumor hypoxia. For PDX 1 a reduced number of tumors were analyzed because of technical problems which hampered CA9 immunostaining. In PDX 3, no tumor masses were detected in samples from olaparib and combination groups, due to the high effectiveness of these treatments.
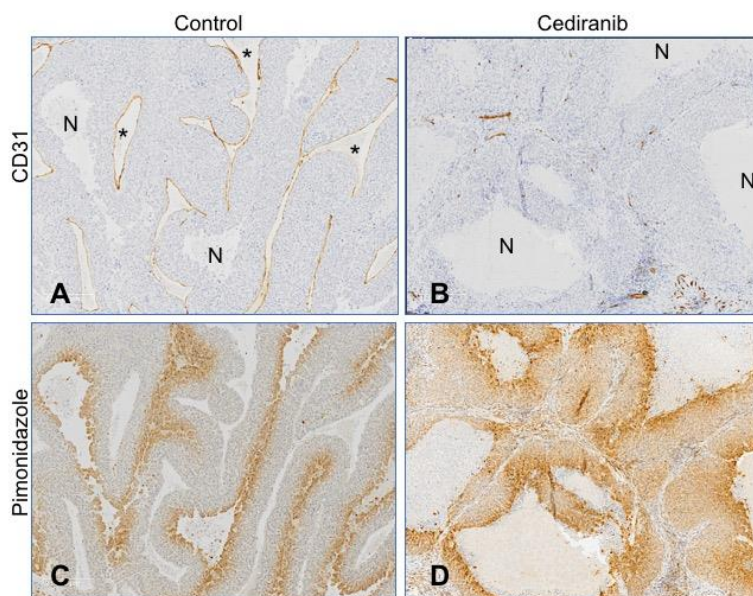

FIGURE 1.9 – PDX 3, illustrative images of immunohistochemical staining for CD31 (A and B) and for Pimonidazole (C and D), from a tumor of the control group (A and C, same microscopic field) and cediranib group (B and D, same microscopic field). 50x magnification.
N=necrotic areas; *=blood vessels lacunae.
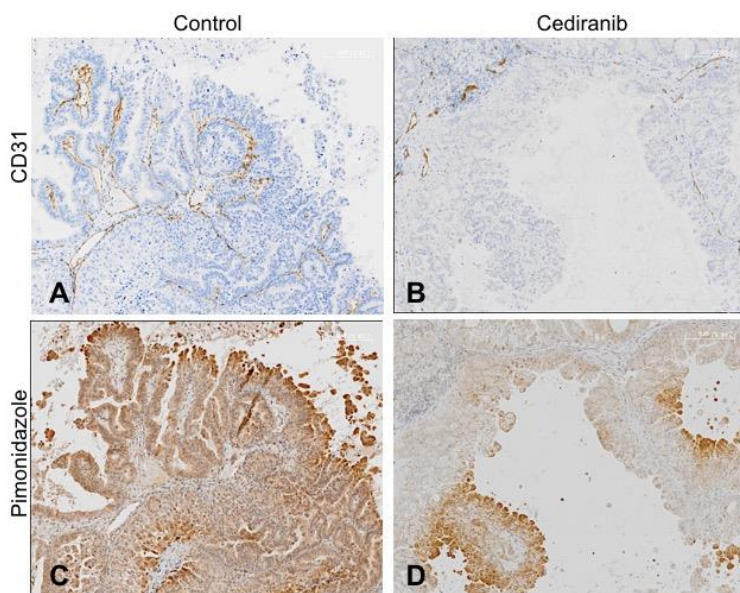
FIGURE 1.10 – PDX 2, illustrative images of immunohistochemical staining for CD31 (A and B) and for Pimonidazole (C and D), from a tumor of the control group (A and C, same microscopic field) and cediranib group (B and D, same microscopic field). 50x magnification.

Intraperitoneal model. The intraperitoneal model was evaluated at sacrifice (established by clinical discomfort evaluation; different day for each mouse). At sacrifice, mice presented moderate to abundant peritoneal effusion (fig. 1.6 F) and at necropsy, multifocal tumoral masses were disseminated on the peritoneal surface of different abdominal organs (carcinomatosis). Mice from cediranib and combination groups, had higher metastatic burden (fig. 1.6 G), mirroring the longer survival time of mice from these groups, and lower amount of ascites compared to controls and PARPi, thanks to the effect of cediranib in reducing vascular permeability.

Blood vessels were reduced by the antiangiogenic treatment (alone or in combination), and the hypoxic levels roughly mirrored the ascites burden. This finding could be related to the compression on large blood vessels produced by the peritoneal effusion which produce systemic blood stasis, impaired tissues perfusion and increased hypoxia.

Conclusions

In conclusion, in the present experiment, histopathological analysis allowed to evaluate the direct effects and the sensitivity of different tumoral models to the antiangiogenic treatment.

Moreover, the administration of the combination demonstrated a promising effect in reducing tumoral growth both in BRCAness and not-BRCAness tumors. The improvement in survival given by the combination compared to the single treatments was possibly due to several mechanism, including summation of the single effects of the two drugs, as well as a sensitization of tumoral cells to olaparib by the cediranib. Recently Kaplan et al. (2019) [37] demonstrated that cediranib confers sensitivity to olaparib through two distinct mechanisms. In particular, a direct effect by inhibiting PDGFR and consequently suppressing the expression of DNA-repair genes, and an indirect effect mediated by the well-known anti VEGFR2 activity of cediranib which induces hypoxia, which secondarily downregulates homology-directed DNA repair (HDR) genes BRCA1/2 and RAD51. The first effect is likely responsible for the efficacy of the combination also in our models in which an increase in hypoxia was not seen upon cediranib administration (PDX2 and PDX5).

Chapter 2 - The Tumor Immune Microenvironment

2.1 Introduction

The notion of anti-tumor immunity was first introduced by Paul Ehrlich in 1909, stating "in the enormously complicated course of fetal and post-fetal development, aberrant cells become unusually common. Fortunately, in the majority of people, they remain completely latent thanks to the organism's positive mechanisms" [38]. The *organism's positive mechanisms* mentioned by Ehrlich were then extensively studied since 1950s until now.

Initially emerged the theory of immunosurveillance, indicating the patrolling role of the immune system, able to recognize and destroy raising neoplastic cells. The major effector cells in immunosurveillance are NK cells, macrophages and cytotoxic T lymphocytes (CTLs).

However, the evidence that also immunocompetent people develop tumors led to the theory of cancer immunoediting. Cancer immunoediting refers to the selection of tumor subclones, able to escape the destruction from immune system [39]. This process evolves over 3 different phases:

- Elimination: is the "immunosurveillance" phase, during which both innate and acquired immunity control the development of nascent cancer cells, destroying them.
- Equilibrium: during this phase, the adaptive immune system controls cancer cell outgrowth and maintain tumor cells in a latent state of dormancy. However, during the equilibrium phase, the immune system exerts a selective pressure on cancer cells, shaping their immunogenicity.
- Escape: which often corresponds to the clinical manifestation of the tumor and is characterized by tumor outgrowth thanks to the ability of tumor cells to circumvent immune system mechanisms. The evolution from the equilibrium to the escape phase, can occur because of decrease antigenicity of the tumor or because of a decrease efficacy of immune system function, frequently due to the secretion by tumor cells or cells from the tumor microenvironment (TME) of immune suppressant factors.

A strong evidence supporting cancer immunoediting is the observation that tumors spontaneously arose in immunodeficient mice are more immunogenic ("unedited tumors") compared to similar tumors arose in immunocompetent hosts ("edited tumors") [40].

During the equilibrium phase, tumor cells develop several different strategies to evade the immune response. These can be generally categorized in two different mechanisms: evading or suppressing the immune system.

Evasion from the immune system is mainly accomplished by two mechanisms: i) the selective overgrowth of antigen-negative tumor cell subclones, which are therefore not recognized by acquired immunity and ii) loss or reduced expression of MHC I molecules and antigen presentation. Immune system suppression is supported by i) secretion of immunosuppressive molecules (e.g. TGF-β, galectins, PGE_2,...) by tumor cells or cells of the tumor microenvironment; ii) promotion of regulatory T cell activity; iii) activation of immunoregulatory pathways (immune check-points) [41].

2.1.1 Pro-tumorigenic inflammation

Despite the above-mentioned role of immunity to be the main endogenous mechanism in controlling tumor growth, immune-inflammatory cells have been described to display also pro-tumorigenic effects during the different stages of tumor development, progression and metastatic dissemination.

Inflammation & Tumor Initiation. Despite the difficulties in investigating the role of inflammation at the very early stages of tumor development, mainly because of the paucity of animal models, the fostering role of inflammation in tumor development is largely accepted. Accordingly, the role of chronic inflammation has been highlighted as one of the major risk factors for the development of most tumor types [42]. The causes of the underlying chronic inflammation are diverse and depends on infectious agents (e.g. *Helicobacter pylori* in the development of gastric lymphomas), idiopathic or immune-mediated inflammatory diseases (e.g. inflammatory bowel disease in colorectal cancer) or exogenous/environmental pollutants (e.g. cigarette smoke and air pollutants in lung cancer). The main mechanism which links inflammation and cancerogenesis is the DNA damage and genomic instability caused by the oxidative stress occurring in the inflammatory microenvironment [43]. DNA damages accumulate due to inhibition of DNA mismatch repair enzymes by random mutagenesis affecting specific genes involved in DNA repair or by direct inhibition of these enzymes by reactive oxygen species. Moreover, the inflammatory microenvironment is enriched of growth factors and cytokines which promote cell proliferation, potentially amplifying occurred random mutations and favoring the acquisition of additional mutations.

Inflammation & Tumor Promotion. Inflammation is involved also in tumor promotion and can be responsible for re-activation of latent premalignant lesions. During tumor promotion, inflammation supports cancer cells with additional growth factors and promotes neoangiogenesis [44]. Tumor-promoting cytokines produced by immune-inflammatory cells can activate transcription factors that stimulate several mechanisms involved in tumor aggressiveness, such as cell survival, proliferation and invasiveness. For example, NF-κB and STAT3 are two transcription factors frequently activated in a number of cancers. Their activation is rarely dependent on direct mutations, but rely on microenvironmental stimuli, such as cytokines produced by tumor-infiltrating immune-inflammatory cells [45,46]. Immune-inflammatory cells influence also tumor neoangiogenesis, a driving force in tumor progression. In particular, tumor associated macrophages (TAMs) mediate hypoxia-induced angiogenesis, by sensing hypoxic stimuli and producing chemokines and proangiogenic factors [47,48].

2.1.2 Innate immune cell populations in the immune microenvironment

Macrophages. In recent years, the pivotal role of tumor associated macrophages (TAMs) gained progressive relevance. Plasticity and diversity are hallmarks of macrophages and two main polarization states of macrophages have been described, in relation to different activating stimuli [49]: M1- (classically activated macrophages) and M2-polarized macrophages (alternative activated macrophages), which display different roles in both inflammatory and tumoral contexts, are not two separate entities, but represent the two extremes of a continuous spectrum of possible activation states. In tumoral contexts, TAMs generally present a M2 phenotype, which is oriented towards promoting tumor growth, remodeling tissues, stimulating angiogenesis and suppressing adaptive immunity [50]. On the contrary, M1-polarized macrophages are, in most tumors, related to a tumor-antagonizing activity [50].

Natural Killer cells. NK cells are key effectors of the innate immunity and tumor immunosurveillance, presenting high potential in killing cancer cells through an antigen-

independent cytotoxic mechanism of action [51]. Accordingly, many studies associated high numbers of infiltrating NK cells to a favorable outcome [52,53], even though it should be underlined that the sole presence of NK cells is not directly related to their ability to exert their tumor-killing function. Indeed, it has been frequently observed that tumor infiltrating NK cells have an anergic phenotype due to the release of suppressing factors (e.g. TGF-β) by tumor cells [52]. Accordingly, it is likely that NK cells can exert their protective role during the very early stages of primary tumor development or metastasis establishment and have little effect in full-developed tumors.

Neutrophils. Similarly to macrophages, also tumor associated neutrophils (TANs) were described to have a dual role in influencing tumor behavior. Indeed, TANs can promote tumoral cell killing through the release of reactive oxygen species (ROS) and neutrophil elastase (NE), inhibit metastatic dissemination and stimulate anti-tumor T cell response by inhibiting TGF-β pathway. On the other hand, production of ROS by neutrophils has been linked to genomic instability and tumor initiation, in association with induction of cell proliferation by NE. Moreover, neutrophils are also involved in the angiogenetic switch and extracellular matrix remodeling (e.g. through the release of MMP-9) which can facilitate cancer cell invasion and metastasis [54].

2.1.3 Anti-tumor adaptative immunity: the "cancer-immunity cycle".

As previously mentioned, tumor cells express a series of non-self antigens which can be recognized by the adaptative immune system during the so-called "cancer-immunity cycle" [55], described in figure 2.1 and analogous to the well-known activation mechanisms of the adaptative immune system in anti-microbial response. However, the cancer-immunity cycle works imperfectly and only rarely leads to the eradication of tumors. Impairment of its efficacy is due to a variety of mechanisms leading to i) lack of activation of the cancer-immune cycle because of downregulation of MHC I-associated presentation of tumor antigens; ii) the inability of T cells to reach and infiltrate the tumor (e.g. abnormal chemokine production in the TME or abnormal expression of ligands on endothelial cells impairing T cells extravasation); iii) T cells anergy and stimulation of regulatory T cells (T_{reg}) (e.g. due to immaturity or impaired function of DCs; immune-check point activation by PD-L1 expression; soluble factors, stromal cells and suppressive leukocytes inhibiting immune functions or impairing T cell activity) [56].

Re-establishing the correct functioning of cancer-immune cycle is the aim of cancer immunotherapy. Current immunotherapy approaches aim at targeting the different aforementioned mechanisms which induce immunotolerance [57]; in particular:

- Cancer vaccines to enhance antigen presentation and stimulate the adaptative immune response;
- Cytokines (e.g. IL-2, IFN, IL-15, …) that promote effector T cell proliferation and activation. Moreover, variation of cytokine landscape can influence tumor proliferation and apoptosis.
- Immune check-point inhibitors, such as inhibitors of the PD1/PD-L1 axis or anti-CTLA4. This class of molecules targets and inhibits such pathways which downregulate the antitumor immune response.
- Other strategies, such as oncolytic viruses and immune cell therapy (i.e. CAR T cells).
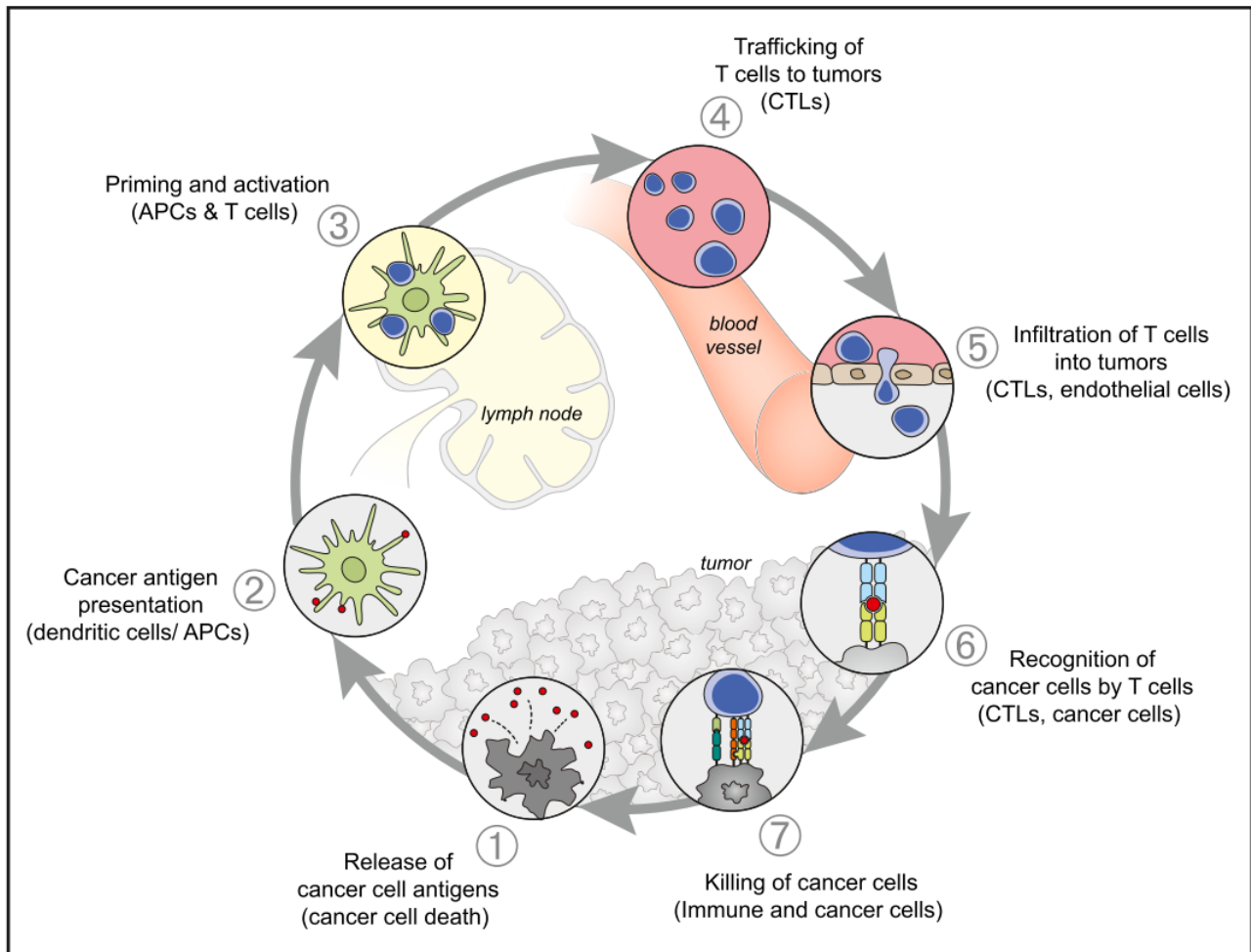
FIGURE 2.1 – The cancer-immunity cycle. Neoantigens are released from tumor cells (1) and recognized by APCs (2). Antigens are presented on MHC I and MHC II to T cells which are in turn activated (3), move to and infiltrate the tumor (4-5). Within the tumor, T cells recognize cancer cells and bind to them through interaction of TCR and the MHC I-antigen complex on tumor cell (6) and exert their killing activity (7). Tumor cell lysis promote the release of additional antigens. Abbreviations: APC= antigen presenting cell; MHC I/II= major histocompatibility complex I/II; TCR=T cell receptor; CTL= cytotoxic T lymphocytes. Image source: Chen & Mellman, 2013 [55].

2.2 Experimental studies

STUDY IV – Target therapies for the treatment of human synovial sarcoma: histopathological analyses in a preclinical study

The present study was conducted in collaboration with the Molecular Pharmacology Unit, Fondazione IRCCS Istituto Nazionale dei Tumori (Milan, Italy). For further details refer to appendix I, publication #2.

Synovial sarcoma (SS) accounts for 8-15% of all soft tissue sarcomas in humans and occurs more commonly in adolescents and young adults [58,59]. The standard of care for synovial sarcoma is resective surgery in association with chemo- or radiotherapy. These treatments represent valuable approaches for localized tumors but fail to success when applied to patients with already developed distant metastases, which represent about 50% of the patients. Indeed, 5-year survival rate for patients with metastatic disease is about 20% [59,60]. Moreover, another important issue, common to several other neoplastic entities is that in the last 20 years, very few improvements have been made in increasing the overall survival (OS) of these patients [59,60]. Accordingly, novel therapeutic strategies are needed in order to improve the OS of patients with metastatic disease. In this scenario target therapies represent valuable emerging approaches in clinical oncology.

The aim of this study was to investigate the therapeutic benefit derived from the combination of a tyrosine kinase inhibitor (TKI) and a heparanase-inhibitor for the treatment of synovial sarcoma.

The TKI chosen for the present study was BMS, an inhibitor of the insulin growth factor 1 receptor (IGF1R), receptor known to be overexpressed in a high proportion of SSs [61,62]. When activated, IGF1R promotes cell proliferation, cell motility and blocks apoptotic signaling pathways. Accordingly, inhibiting IGF1R and the downstream signaling pathways might represent a promising strategy to antagonize tumor progression.

Heparan sulfates (HS) constitute the lateral chains of heparan-sulfate proteoglycans, which are involved in cell-cell and cell-ECM interaction, modulating tumor behavior primarily inhibiting cell invasiveness. Heparanases are enzymes able to cleave HS, producing biologically active HS fragments, which can promote several biological processes, such as cell proliferation and angiogenesis, sustaining tumor growth [63]. Heparanases are normally present only during fetal development but have been noted to be overexpressed in several tumor types, including synovial sarcomas, thus representing optimal target for anticancer therapy.

In the second instance we investigated the immune-modulatory effects of these therapies in a metastatic setting.

Materials and methods

In vivo experiment. 34 SCID mice were inoculated within the thigh muscles with a synovial sarcoma cell line of human origin (CME-1), which spontaneously metastasizes to the lung. 5 days post-injection, mice were randomized in 4 groups of treatment (tab. 2.1). Tumoral growth was monitored as reported in appendix II and mice were sacrificed when the mean tumoral volume of each the treatment group was approximately 2000 mm^3.

TABLE 2.1 – Experimental groups.

Group	Treatment
Control	Vehicle
ssLMWH	Heparanase-inhibitor
BMS	Tyrosine kinase inhibitor (BMS754807)
Combination	Combination of ssLMWH and BMS754807

Histopathology. At necropsy, the left lung from each mouse was formalin fixed and paraffin embedded for histopathology. Serial sections from each lung were stained with Hematoxylin and Eosin and by immunohistochemistry with the primary antibodies listed in table 2.2. All the histological slides were digitalized with a slide scanner (Nanozoomer, Hamamatsu) for whole slide image analysis.

The metastatic burden was assessed by counting the number of metastatic nodules on MHC I stained slides. The immune-inflammatory infiltrate (mononuclear-phagocytes, neutrophils and natural killer cells) was evaluated in its spatial distribution and quantified by using digital image analysis with ImageJ software (appendix VII). Results are expressed as percentages of immunopositive area on the total parenchymal area. Immunohistochemistry for cleaved caspase-3 was performed to further characterized metastatic nodules (tab. 2.2).

Histopathological evaluation was performed blinded (i.e. without knowledge of the treatment group).

Statistics. Normal distribution of data was evaluated with Kolmogorov-Smirnov test. Differences among groups were analyzed with Mann Whitney or Kruskal-Wallis nonparametric tests. Differences were considered significant when $p < 0.05$.

TABLE 2.2 – List of primary antibodies (see appendix III and IV for details).

Marker	Specificity
Human MHC I	Cells of human origin
Iba1	Cells of the mononuclear-phagocytic system
Ly6g	Neutrophils
NKp46	Natural Killer cells
Cleaved Caspase-3	Apoptotic cells

Results

Both ssLMWH and BMS significantly delayed tumoral growth compared to the control group. Further benefit derived from the combination of the two compounds, which was able to almost completely inhibit tumor growth (fig. 2.2 A). Similarly, the metastatic burden was considerably lower in ssLMWH and BMS groups, and further reduced in the combination group (fig. 2.2 B and C).

Concerning the inflammatory infiltrate, digital image analysis demonstrated an increase of the 3 immune-inflammatory cell populations (mononuclear-phagocytes, neutrophils and natural killer cells) in the ssLMWH and the combination groups. This trend was not statistically significant (fig. 2.3 A).

Moreover, the spatial distribution of the 3 cell populations was investigated (fig. 2.3 B): numerous Iba1+ cells infiltrated both the large and small metastatic nodules; neutrophils slightly infiltrate tumoral masses and were mainly distributed in the surrounding parenchyma. On the contrary, rare, if any, NK cells were present within tumoral masses, but scattered aggregates of NK cells were observed multifocally throughout the lung parenchyma, particularly in mice from the combination group.
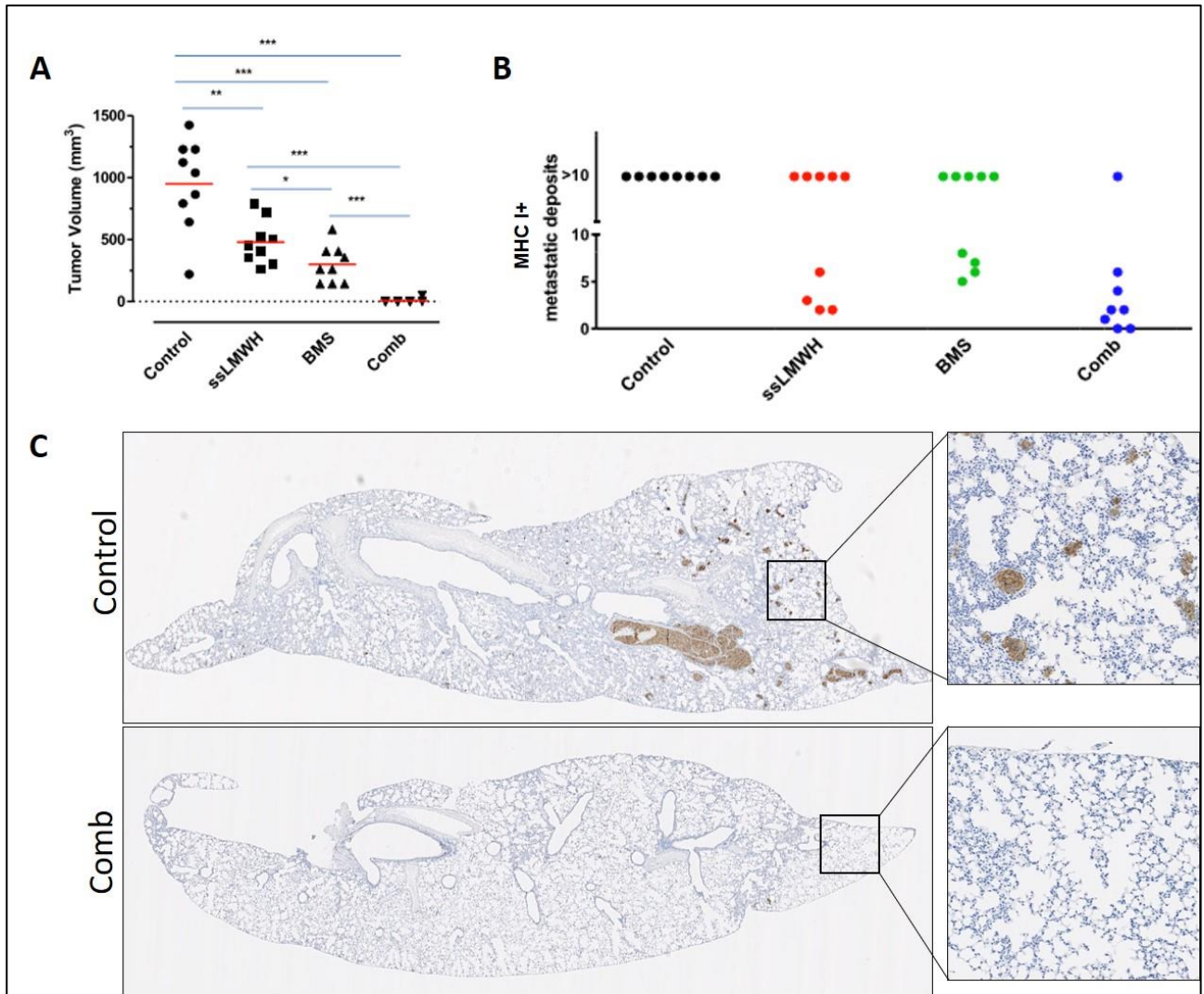
FIGURE 2.2 – A) Primary tumor volume at 30 days post injection. B) number of MHC I+ metastatic nodules. C) representative images of the pulmonary metastatic burden of the control and combination group. IHC for human MHC I, whole lung section; inset: 100x magnification. Modified from Cassinelli et al, 2018[64].
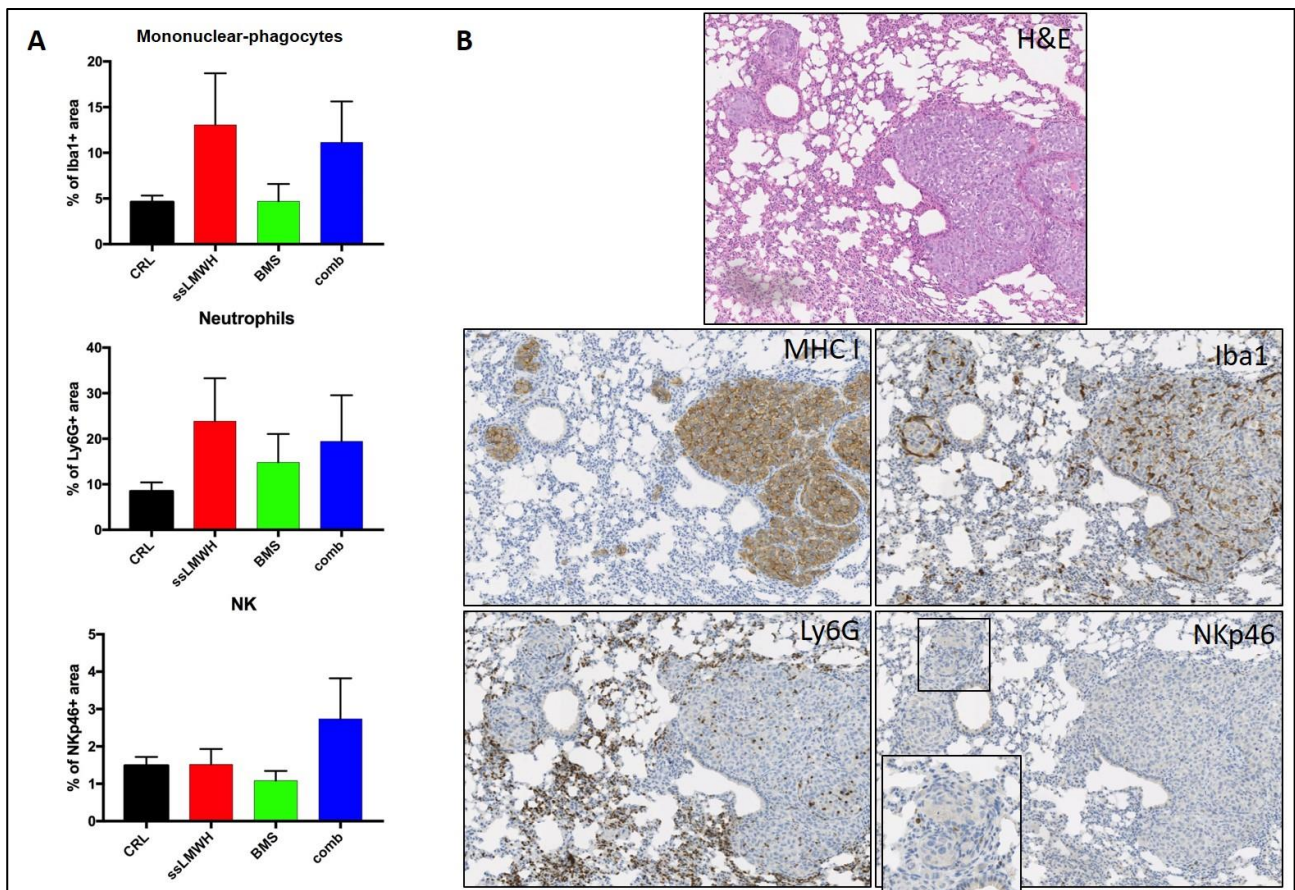
FIGURE 2.3 – A) Immune-inflammatory cell infiltrate in the lung parenchyma: percentage of immunopositive area for the three markers (Iba1, Ly6G and NKp46). B) Representative images of the different stainings, the same microscopic field is shown in the five pictures, stained with H&E and with IHC for human-MHC I (tumoral cells), Iba1 (mononuclear-phagocytes), Ly6G (neutrophils) and NKp46 (natural killer cells). XX magnification, NKp46 inset: 400x magnification.

In all the samples, along with small (<10 cells) and large (>10 cells) well developed metastases, metastatic nodules showing degenerative changes (tab 2.3) were observed and defined as abortive metastases. Moreover, these nodules were characterized by an increased number of apoptotic tumoral cells (fig. 2.4 A). Accordingly, based on the morphological features listed in table 2.3, the percentage of abortive metastases in 10 small metastatic nodules randomly selected from each sample was calculated. Results are shown in fig. 2.5 A and demonstrated a higher number of abortive metastases in the combination group.

The potential relation between abortive metastases and the aggregates of NK cells was further investigated. For each sample 4 metastatic nodules were selected, classified as well-developed or degenerated metastasis and serially evaluated in human MHC I- and NKp46-stained slide. For each nodule, the number of tumoral cells (MHC I+) and NK cells (NKp46+) was counted and the NK/tumoral cell ratio calculated. Results demonstrated that in well-developed metastases, only rare NK cells infiltrated the nodules, while in degenerated ones aggregates of NK cells were present, as demonstrated by a significant increase in NK/MHC I ratio (fig. 2.5 B and C).

TABLE 2.3 – Morphological features of developing and abortive metastatic nodules.

Feature	Developing metastasis	Abortive metastasis
Cell architecture	Closely packed cells /organized in a nodular mass	Neoplastic cells separated /infiltrated by MHC I negative cells
Cell borders	Regular and distinct	Irregular, indented and poorly defined
Nuclei	Normally shaped and homogeneously distributed chromatin	Condensed chromatin/ pyknosis
Apoptotic bodies	Absent	Present
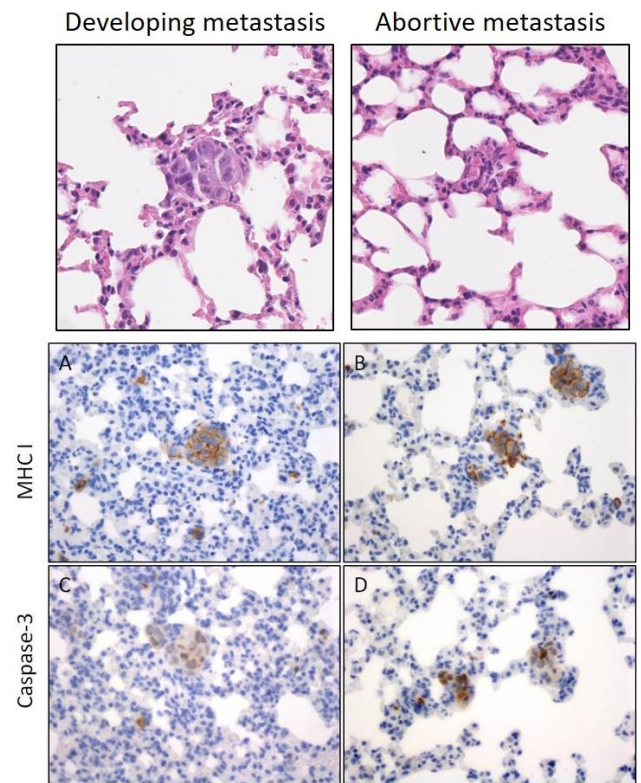
FIGURE 2.4 – Morphological differences between developing and abortive metastases.
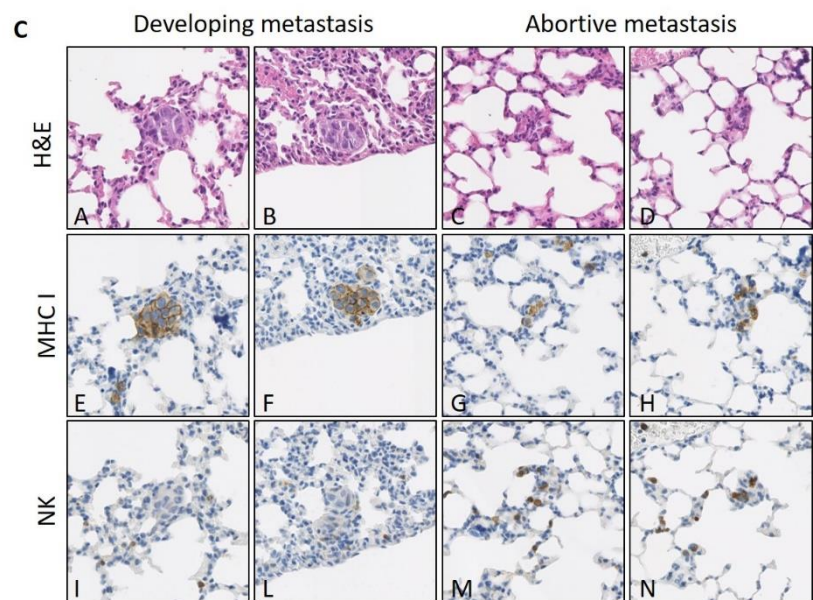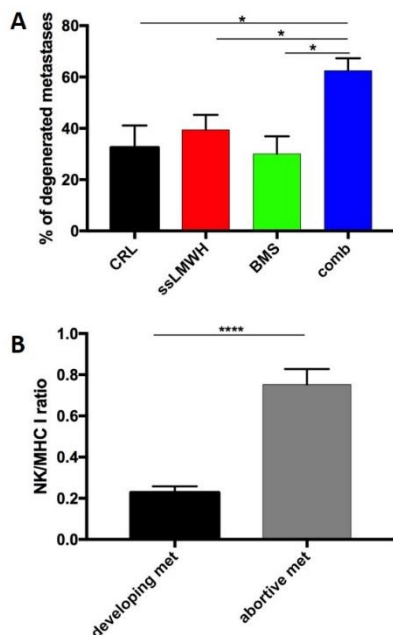
FIGURE 2.5 – Prevalence and characterization of abortive metastasis. A) a significantly higher number of abortive metastases was observed in the combination group compared to controls and single treatment groups. B) Abortive metastases were characterized by few MHC I+ cells (tumoral cells) and higher number of NK cells, compared to developing metastases. C) representative images of developing and abortive metastasis, showing different morphological features and different MHC I/NK ratio. H&E and IHC for human MHC I and NKp46. Original magnification 400x. Modified from Cassinelli et al., 2018 [64].

Conclusions

The present study demonstrated the potential benefit derived from the combination of a receptor tyrosine kinase inhibitor and an HS mimetic/heparanase-inhibitor in the treatment of human synovial sarcoma. Moreover, the obtained results suggest an immunomodulatory effect of the treatments showing the potential role of NK cells in hindering neoplastic cell engraftment in a very early phase of metastatic dissemination. The peculiar distribution of NK cells and in particular their association with degenerating metastatic nodules (abortive metastases) is indicative of an involvement of NK cells in the mechanism of action of ssLMWH. This finding is supported by a recent publication [65] which demonstrated, in a syngeneic model of lymphoma, intratumoral NK cell recruitment and their activation upon the administration of a HS mimetic and their role in antagonizing tumor growth.

STUDY V – Macrophage populations in experimental models of thyroid cancer

The present study was conducted in collaboration with the Molecular Mechanisms Unit, Fondazione IRCCS Istituto Nazionale dei Tumori (Milan, Italy).

Thyroid carcinoma is the most frequent endocrine neoplasm in humans, accounting for approximately 1.5% of all human cancers. Most of thyroid carcinomas (except for medullary carcinoma) originate from the follicular epithelium and are classified in 3 histological variants: papillary carcinoma (PTC) accounting for more than 85% of cases, follicular carcinoma (FTC, 5-15% of cases) and anaplastic carcinoma (ATC, <5% of cases). While PTC are usually characterized by a favorable prognosis with an overall 5-year survival of more than 90%, the outcome for ATC is poor, and most of the patients die in less than 1 year from diagnosis and no effective therapies are presently available.

As in several other neoplastic entities, there is a strict interplay between thyroid tumors and immune-inflammatory cells that populate the TME. Among others, the role or tumor-associated macrophages has been extensively studied in thyroid carcinoma. Increased density of TAMs has been observed in thyroid carcinomas compared to benign lesions and it was correlated with negative clinical-pathological parameters in both well differentiated and anaplastic variants of thyroid carcinoma [66,67].

A previous *in vitro* study [68] demonstrated different ability of human cell lines of thyroid carcinoma to induce a M2-phenotype in isolated human monocytes, through a PGE_2-mediated activity. The aim of the present study was to assess the ability of the same thyroid carcinoma cell lines, to reproduce their macrophage-polarizing or non-polarizing activity also *in vivo,* after subcutaneous xenotransplantation of tumoral cells in nude mice.

Materials and methods

5 different cell lines of human origin, derived from papillary and anaplastic thyroid carcinoma, were subcutaneously engrafted in nude mice (tab. 2.4). For each sample, a 3 mm thick sample collected from the central part of the tumoral mass and including the overlying skin, was formalin fixed and paraffin embedded. 4 μm serial sections from each tumor xenograft were routinely stained with Hematoxylin and Eosin and by immunohistochemistry for the markers listed in tab. 2.5. For each marker, the immunostained population was evaluated by a semiquantitative score in two different regions of the tumor: the bulk and the periphery (capsule) of the tumor. Moreover, morphological features of cells labeled by each marker were also considered.

**TABLE 2.4** – Thyroid carcinoma cell lines evaluated in the present study.

Cell line	Subtype	n° of mice
NIM-1	PTC	2
8505-C	ATC	2
HTC-C3	ATC	2
K1	PTC	2
FRO81-2	ATC	2

TABLE 2.5 – List of primary antibodies (see appendix III and IV for details).

Marker	Specificity
Iba1	Cells of the mononuclear-phagocytic system
iNOS	M1 macrophages
Arginase I	M2 macrophages

Results

In general, all the tumors shared the following morphological features: well demarcated unencapsulated nodular mass which expands the subcutis and occasionally infiltrates underlying musculature (fig. 2.6). Neoplastic cells are arranged in solid areas and lobules or cystic structures (NIM-1 cell line), infiltrated by minimal to moderate amount of fibrovascular stroma.
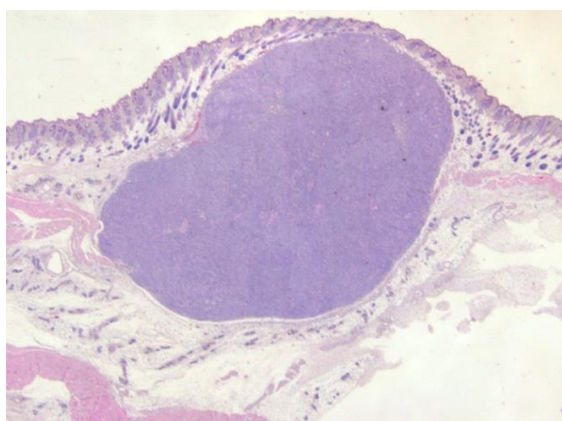
FIGURE 2.6 – representative overview of a subcutaneous xenograft. HTC-C3 cell line, H&E, 25x

Concerning the immunohistochemical staining, a high number of Iba1+ cells was present in all the samples and were widely distributed both in the capsule and the bulk of the tumor. A variable number of Arginase I+ cells was present in most of the samples, mainly localized within the bulk of the tumor, and represented approximately from 10 to over 95% of the Iba1+ cells. On the contrary, iNOS was expressed by rare macrophages but also by a variable percentage of tumoral cells, depending on the cell line considered.
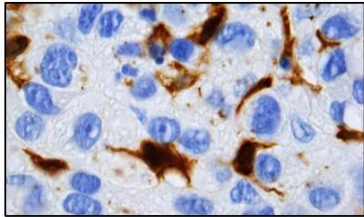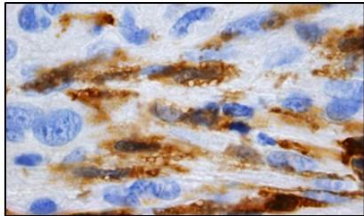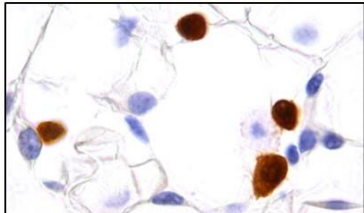
Iba1-positive cells were characterized by three different morphologies (dendritic, spindle and round), differently distributed throughout the tissue (fig. 2.7):

- Dendritic cells infiltrated tumoral lobules and were intermingled with neoplastic cells, with dendrites embracing them.
- Spindle cells were mainly localized within stromal septa and accordingly, higher prevalence of this population was present in the tumors characterized by abundant fibrovascular stroma dissecting the neoplastic mass.
- Round cells were mainly located at the periphery of the tumor or in the surrounding subcutaneous tissue.

Overall, Arginase I+ cells recapitulated the morphology and distribution of Iba1+ cells, while iNOS+ cells were predominantly spindle-shaped and localized within the stroma (exception for tumoral cells which expressed iNOS).

Results from the semiquantitative analysis are reported in table 2.6 and representative images are provided in fig.2.8.

Localization	Shape	
Intralobular	Dendritic	
Stroma	Spindle	
Peritumoral adipose tissue	Round	

FIGURE 2.7 – Morphology and prevalent distribution of Iba1+ cells. IHC for Iba1, original magnification 1000x.
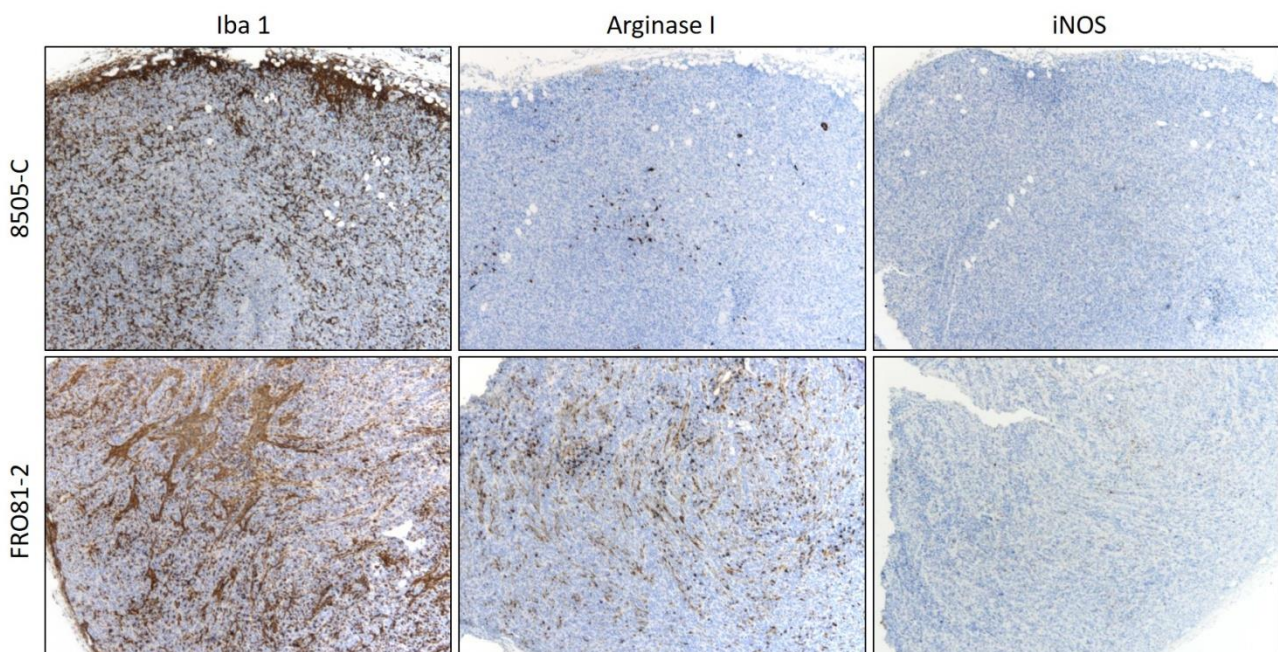
FIGURE 2.8 – distribution, amount and polarization state of TAMs infiltrating a non-polarizing (8505-C) and a polarizing (FRO81-2) cell line. IHC for Iba1, Arginase I and iNOS; original magnification 50x.

TABLE 2.6 – Summary of the results.

Cell line	mouse ID	Iba1		Arginase I		iNOS		
		periphery	bulk	periphery	bulk	periphery	bulk	tumor cells
NIM-1	#1	+ D +/++ S	++ D - S	- D + S	+ D - S	-	-	+ (diffuse, weak)
	#2	+ D ++ S	++ D -/+ S	- D -/+ S	+/++ D - S	-	-	+ (scattered, intense)
8505-C	#1	+ D ++ S	+++ D + S	- D + S	-/+ D - S	-	-	+ (scattered, intense)
	#2	++ D +++ S	+++ D + S	- D - S	-/+ D - S	-	-	+ (scattered, intense)
HTC-C3	#1	++ D ++ S	++ D +++ S	- D + S	-/+ D +/++ S	- D + S	- D ++ S	+ (scattered, intense)
	#2	+ D ++ S	++ D +/++ S	- D -/+ S	-/+ D -/+ S	-	- D + S	++ (patchy, intense)
K1	#1	+ D + S	+++ D ++ S	-	+ D +++ S	-	- D + S	-/+ (scattered, intense)
	#2	+ D + S	+++ D +++ S	-	++ D ++ S	-	- D + S	-/+ (scattered, intense)
FRO81-2	#1	+ D +++ S	+++ D +++ S	-	+ D ++ S	-	-	-/+ (scattered, intense)
	#2	+ D +++ S	+++ D +++ S	-	+ D ++ S	-	- D -/+ S	+ (scattered, intense)

Abbreviations: D=dendritic; S=spindle; R= round;

Conclusions

In general, the 2 samples derived from the same cell line demonstrated similar morphological features and comparable results in the overall amount of tumor-infiltrating macrophages as well as their polarization status.

From previous *in vitro* experiments, HTC-C3, K1 and FRO81-2 cell lines demonstrated to induce an M2 polarization status of human monocytes, while NIM and 8505-C cell lines do not [68]. Similarly, in the present experiment we observed that an overall reduced number of tumor-associated macrophages, either spindle and dendritic in shape, is present within 8505-C and NIM-1 tumors, and that Arginase I-positive spindle cells are drastically reduced compared to the 3 other cell lines, supporting the non-polarizing activity of these cell lines.

A slight decrease in Arginase I-positive dendritic cells was also observed in the 8505-C and NIM-1 tumors. Iba1 is considered a pan-macrophagic marker [69], being expressed by all macrophage populations except for alveolar macrophages. Its expression on dendritic cells is still largely undefined, and some authors claim the expression of Iba1 also in subsets of DCs [70,71]. It is therefore possible that Iba1+ (and Arginase I+) cells with dendritic shape represent intratumor-dendritic cells (DCs) and not tumor-associated macrophages. However, since cell populations immunostained by Iba1 remain to be elucidated, the present finding should be further investigated.

STUDY VI – Immune microenvironment in an experimental model of colon adenocarcinoma

The present study was conducted in collaboration with the Molecular Oncology Unit, Centro di Riferimento Oncologico (Aviano, Italy). For further details refer to appendix I, publication #3.

Colorectal cancer (CRC) is the third most common cancer by incidence, and despite improvements made in patients care, it remains one of the leading cause of cancer-related death, particularly in developed countries [72].

High percentage of CRC are represented by the colitis-associated (CAC) subtype, which pathogenesis is linked to an underlying form of inflammatory bowel disease (IBD). Therefore, the inflammatory microenvironment is supposed to be relevant in the initiation and the promotion of such type of cancer. However, tumor immunity in CAC presents some peculiarities compared to other epithelial tumors. For example, infiltrating T lymphocytes normally have specificity for tumor-specific antigens and consequently have an antitumorigenic activity. On the contrary, in CAC, T lymphocytes are commonly directed against microbial antigens of the intestinal microflora, and thus are unable to kill tumor cells, while promoting a pro-tumorigenic microenvironment by producing inflammatory cytokines [73].

Emilin1 is an extracellular matrix glycoprotein, involved in several diverse physio-pathological processes, including the promotion of adhesion and migration of several cell types [74]. It has been described a tumor-suppressive role of Emilin1, thanks to the downregulation of PTEN pathway with a consequent antiproliferative effect [74].

In previous experiments of DSS induced-chronic colitis performed on wild type and Emilin1 deficient mice, we observed a genotype-related variation of inflammatory populations. This finding prompted us to investigate the role of Emilin1 in a tumoral setting and its relation with the immune cells populations in the development of colorectal cancer.

Materials and methods

In vivo experiment. EMILIN1 wild type (E1$^{+/+}$), knock out (E1$^{-/-}$) and transgenic mice (E1-E933A, expressing a mutant EMILIN-1 unable to interact with the $\alpha_4/\alpha_9\beta_1$ integrins) were generated on a C57Bl/6 background. On day 0, mice were treated with a single dose of the carcinogenic compound azoxymethane (AOM) and two cycle of dextran sulfate sodium (DSS) were administered for 7 consecutive days starting from day 7 and day 28 [75]. Untreated mice from the 3 genotypes were included in the experiment as negative controls.

Histopathology. Mice were humanely euthanized on day 56. Colon were opened to examine the mucosa and the number of masses was recorded. Standard samples from the distal colon were collected, formalin fixed for 24 hours and paraffin embedded. Serial sections from each sample were stained with Hematoxylin and Eosin (H&E) and by immunohistochemistry (IHC) with a panel of primary antibodies for the evaluation of the tumor-infiltrating immune populations (tab. 2.7).

Proliferative colon lesions were classified according to Boivin et al. (2003) [76] grading system. Moreover, the intratumor inflammatory infiltrate was semi-quantitatively scored and any additional pathologic findings were recorded.

Immune cell populations were evaluated on the respective IHC-stained slide. The number of IHC-positive cells was counted in 2 400x microscopic fields within the tumor area, and a value was

assigned according to the scoring system reported in table 2.8. A mean value of the score obtained in the 2 fields was then calculated for each sample and used for further statistical analysis. Iba1 stained slides were evaluated by digital image analysis (appendix VII), measuring the percentage of immunopositive area with image J software. A score was then arbitrary assigned according to criteria reported in table 2.8.

Histopathological evaluation was performed blinded (i.e. without knowledge of the treatment group).

Statistics. Statistical differences between groups were evaluated Mann-Whitney nonparametric test. Differences were considered significant when $p < 0.05$.

**TABLE 2.7** – List of primary antibodies (see appendix III and IV for details).

Antibody	Specificity
CD3ε	T lymphocytes
B220	B lymphocytes
Ly6G	Neutrophils
Iba1	Mononuclear-phagocytic cells

TABLE 2.8 – Scoring system used for the evaluation of IHC.

| Score	Description	
	CD3, B220, Ly6g	Iba1
0	0 positive cells	Negative tissue
1	1-5 positive cells	Iba1+ area <3%
2	6-15 positive cells	Iba1+ area ≥3% and <6%
3	16-30 positive cells	Iba1+ area ≥6% and <12%
4	>30 positive cells	Iba1+ area ≥12%

Results

Any pathological finding was observed in untreated animals, and the colon from the 3 different genotypes showed similar histological morphology (fig. 2.9).
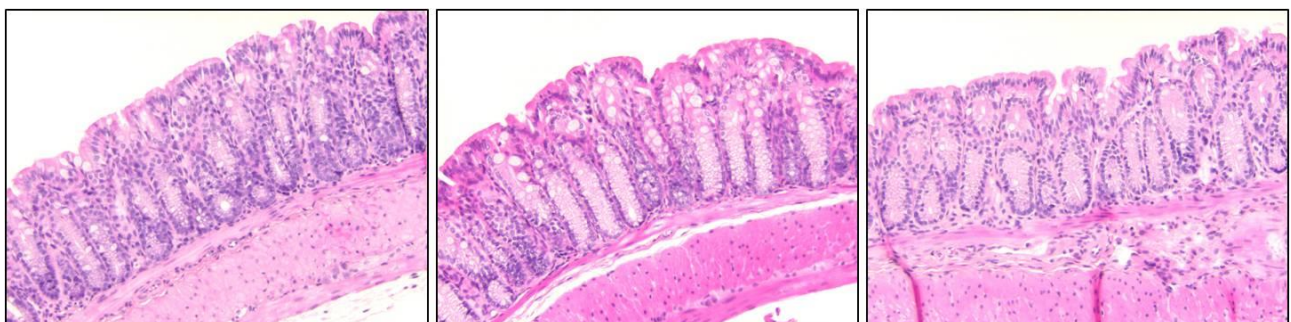

FIGURE 2.9 – Untreated mice from the 3 different genotypes: wild type (left), knock out (middle) and E1-E933A transgenic mice (right). Image from Capuano et al., 2019 [77].

Among AOM-DSS treated mice, the proportion of mice with gross colon lesions was higher in knock out and E1-E933A groups (fig. 2.10 A), as well as the number of masses in each sample (fig. 2.10 B). The observed microscopic lesions are reported in tab.2.9, and in general, E1-E933A mice had more severe proliferative lesions (fig. 2.11 A).

Scoring of the intratumor inflammatory infiltrate demonstrate a higher degree of inflammation in proliferative lesions of E1-E933A transgenic mice (fig. 2.11 B), but any predominant immune cell population was identified by immunohistochemistry (fig. 2.12).
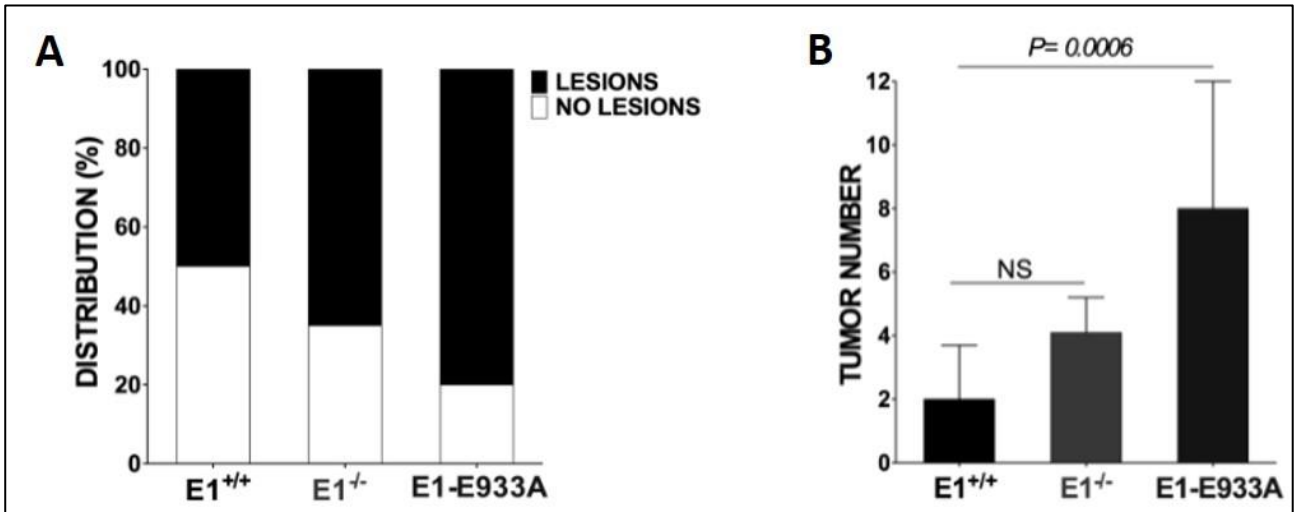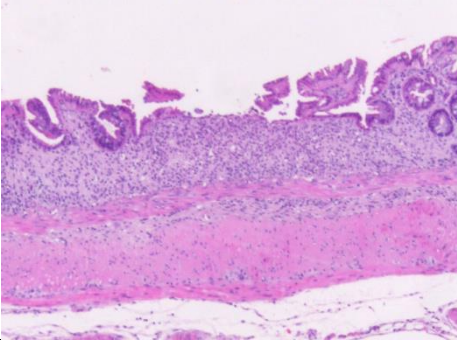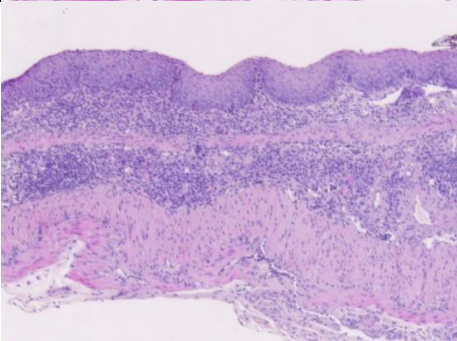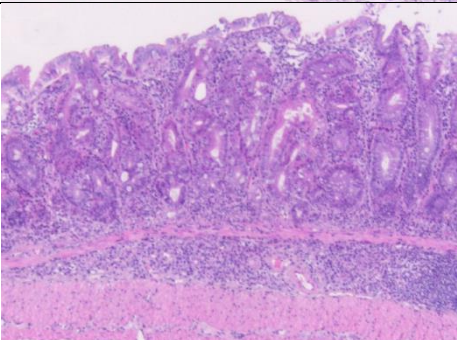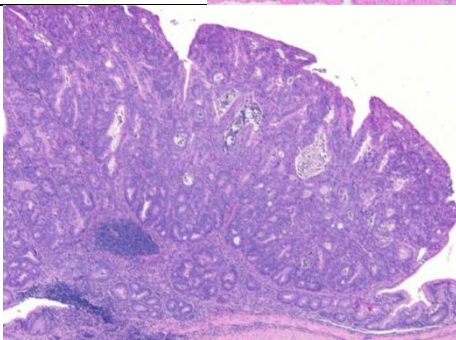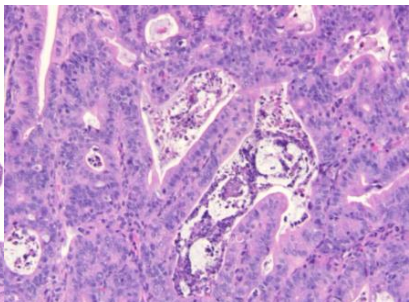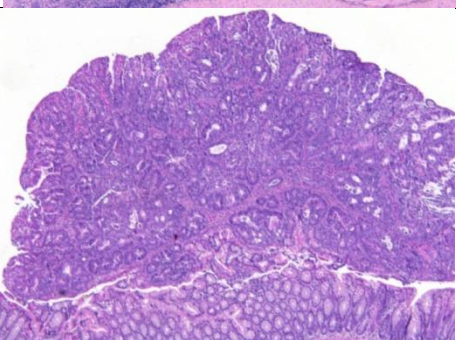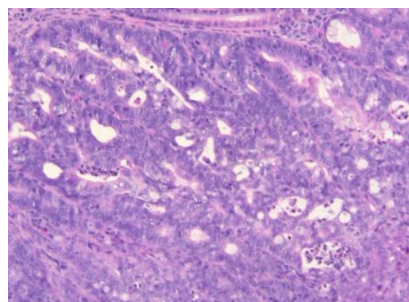
FIGURE 2.10 – Gross findings. A) Higher incidence of macroscopic colon lesions was observed in knock out (E1^{-/-}) and transgenic (E1-E933A) mice. B) In affected mice, the number of masses was significantly higher in transgenic (E1-E933A) compared to wild type (E1^{+/+}) mice. Modified from Capuano et al., 2019 [77].
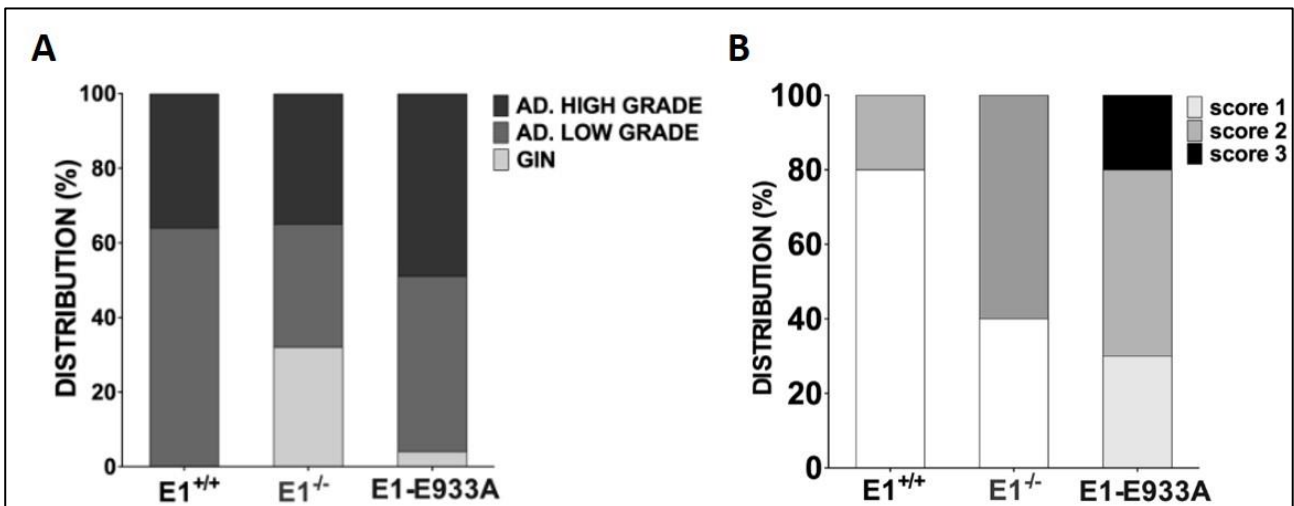
FIGURE 2.11 – Histopathology results. A) Higher prevalence of high-grade adenomas was observed in transgenic (E1-E933A) mice. B) Inflammatory infiltrate within the lamina propria was more severe in transgenic (E1-E933A) and knock out (E1^{-/-}) mice. Abbreviations: AD. =adenoma; GIN=gastro-intestinal intraepithelial neoplasia. Modified from Capuano et al., 2019 [77].

TABLE 2.9 – Classification and representative images of observed lesions.

NON-PROLIFERATIVE LESIONS	Mucosal erosion/ulcer	
	Squamous metaplasia	
PROLIFERATIVE LESIONS	Gastro-intestinal intraepithelial neoplasia (GIN)	
	Low-grade adenoma	
	High grade adenoma	
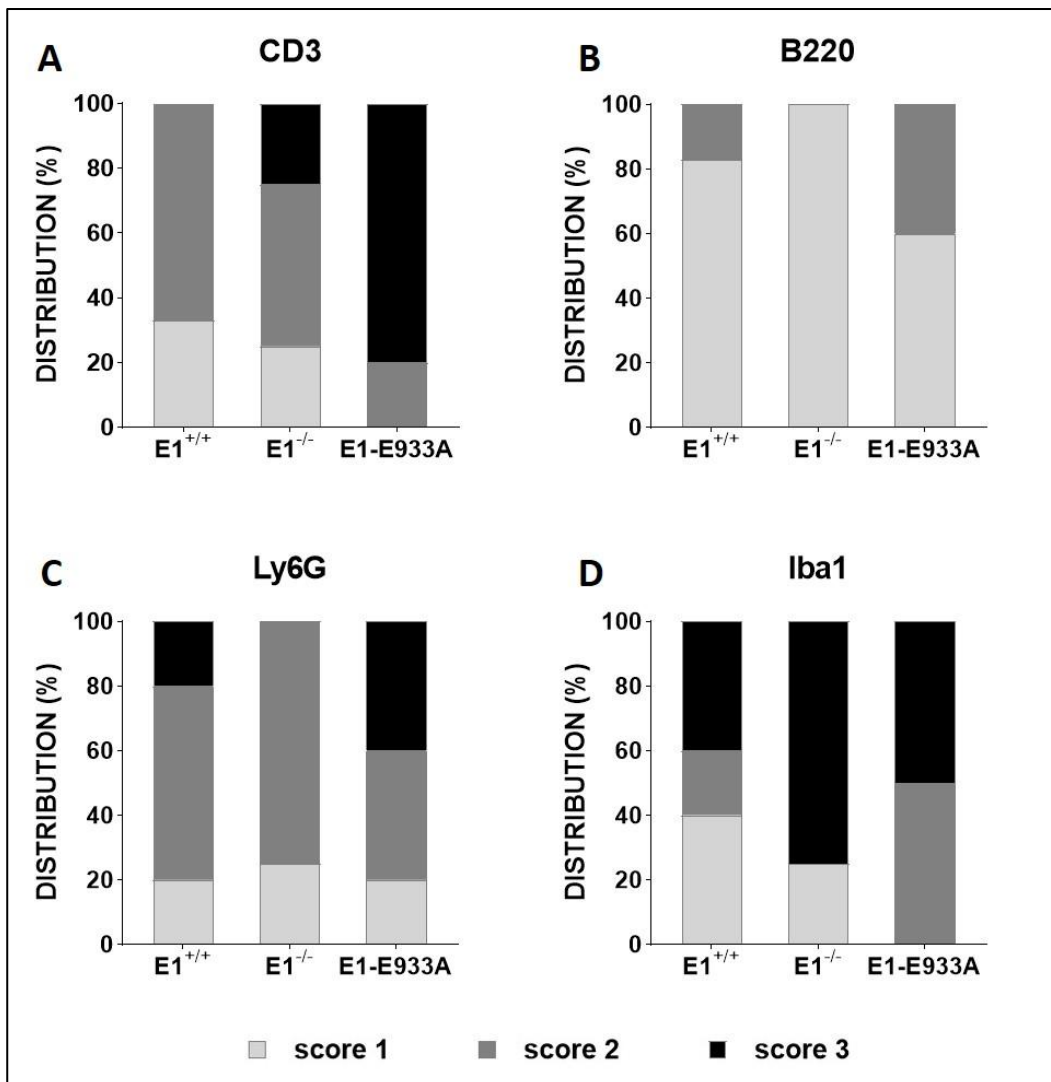
FIGURE 2.12 – Immunohistochemistry results.

Conclusions

In the present study, a broad range of pathological conditions were encountered upon AOM-DSS administration. Mice presented high variability in the severity of the lesions observed, ranging from mild (inflammation and mucosal erosion) to severe conditions (tumoral lesions).

Squamous metaplasia of colon mucosa after DSS administration has been reported as a strain-related condition, with higher frequency described in C57Bl/6 [78]. This finding is most likely related to a re-epithelization of the damaged distal colon mucosa by rectal epithelial cells proliferation [78].

The higher tumoral burden observed in E1-E933A mice compared to E1^{+/+} mice, supports previous results indicating an antiproliferative activity of EMILIN-1 [74]. In addition to previous findings showing a pro-inflammatory activity of mutant EMILIN-1 in a chronic colitis model, the increased intratumor inflammatory infiltrate observed in mutant E1-E933A mice, suggests a potential role of EMILIN-1 in the pathogenesis of CAC. Nevertheless, any specific inflammatory cell population that could predominantly drive tumorigenesis was identified.

Chapter 3 - Tumor Stroma

3.1 Introduction

Stroma is defined as the supporting framework of parenchymal organs and is constituted by two main components: fibroblasts (the cellular component) and the extracellular matrix (ECM). As in normal organs, in solid tumors, the stroma provides the scaffold for neoplasms to grow and accommodates infiltrating cells (i.e. immune-inflammatory cells) and the vascular network. However, tumoral stroma is not a passive bystander, but perpetually undergoes remodeling processes (stromal activation) and interacts with cancer cells and the other components of the tumor microenvironment (TME), influencing tumor development and progression.

In 1980s Dvorak defined tumors as *wounds that do not heal* [79], recognizing the striking similarities between tumoral stroma and chronic wound healing. Indeed, in full developed organs, in physiological states, the supporting stroma is characterized by a moderate number of resting fibroblasts (fibrocytes) embedded in an ECM, which homeostasis is mainly maintained by a balanced activity of matrix metalloproteases (MMPs) and their inhibitors (TIMPs). During wound healing, as well as in tumors, the number of fibroblasts drastically increases, and they acquire new morphological and functional features (fibroblasts activation). Activated fibroblasts are characterized by stellate shape, plump nucleus, increased proliferation, acquired migratory capacity, and increased synthesis and deposition of ECM. From a molecular point of view, activated fibroblasts are characterized by the expression of α-SMA (for this reason they are also referred to as myofibroblasts), PDGFRβ and fibroblast activation protein (FAP). Recruitment and activation of fibroblasts rely on different growth factors, chiefly TGFβ, but also PDGF and FGF2 [80].

The ECM is the non-cellular component of the stroma and is predominantly composed of fibrous proteins (FPs) and proteoglycans (PGs). Fibrous proteins are mainly represented by collagens and to a lesser extent by elastin and fibronectins. FPs are the main structural components of ECM and confers tensile strength and regulate cell adhesion and migration [81]. Proteoglycans are glycoproteins, covalently linked to lateral glycosaminoglycan (GAG) chains. In the ECM, PGs are in the form of a hydrated gel and thanks to their high negative charge can bind large amount of water, maintaining tissue hydration, double-charged cations and can sequester biologically active molecules, such as growth factors [81].

ECM homeostasis is maintained by continuous degradation and production of its components (remodeling), fundamental to regulate its abundance, composition and structure, as well as release of growth factors usually sequestrated in its meshwork. ECM remodeling is exerted by a balanced activity of proteolytic enzymes [82], and in particular:

- Matrix metalloproteases (MMPs): a family of zinc-dependent enzymes are the major class of ECM remodeling enzymes. MMPs are usually secreted as inactive zymogens and can be in soluble or membrane-anchored form. The activity of MMPs is characterized by substrate specificity, but collectively MMPs can degrade all ECM proteins.
- Adamalysins (ADAMs): a family of membrane-anchored proteins, closely related to MMPs. ADAMs cleave and release, extracellular domains of transmembrane proteins, releasing active fragments of cytokines and GFs, and adhesion molecules, regulating cell-ECM interaction. Some ADAM-family members (ADAM-10, ADAM-12 and ADAM-15) can also cleave ECM fibrous proteins such as collagens.

- Tissue-inhibitors of metalloproteases (TIMPs): a family of proteins composed of 4 members (TIMP1-4), which inhibit the activity of ECM-degrading enzymes, such as MMPs and ADAMs, with a certain degree of specificity for the substrate.

The importance of the fine regulation of this process became evident from the variety of diseases involving dysregulated ECM breakdown or excessive deposition in their pathogenesis, such as cardiomyopathies, osteoarthritis, cartilage degradation and organ fibrosis.

3.1.1 Role of tumor stroma in cancer

Activated fibroblasts within a tumor are named cancer-associated fibroblasts (CAFs). CAFs are involved in several mechanisms that allow and promote cancer growth and invasion. Contrary to normal fibroblasts, that have been demonstrated to inhibit tumoral cell proliferation [83], CAFs promote survival and replicative ability of cancer cell through the secretion of a variety of mitogenic and anti-apoptotic signals (e.g.IGF-1 and IGF-1, EGF, FGF…) or sustain angiogenesis via the secretion of VEGF and FGF family members.

CAFs are also responsible for the production of TGFβ and other chemoattractants and activators of macrophages and other myeloid cells, thus stimulating an immune suppressive microenvironment which in turn can sustain tumor cell proliferation and aggressiveness. CAFs are also involved in the metastatic process, thanks to their ability to promote a mesenchymal shift in cancer cell phenotype (epithelial to mesenchymal transition, EMT), mediated by TGFβ production or E-cadherin cleavage which enable the acquisition of an invasive phenotype [84]. Moreover, the activity of CAFs in the remodeling of extracellular matrix is also responsible for structural modifications of ECM which can favor tissue invasion and metastatic dissemination to distant organs of cancer cells.

Similarly, the ECM represents an extraordinary source of molecules which can be released in soluble forms during ECM remodeling and which intervene in the complex network of the tumor microenvironment, modulating inflammation, angiogenesis and tumor cell proliferation and survival.

3.2 Experimental studies

STUDY VII - Identification and preliminary validation in mouse models of circulating biomarkers of pancreatic ductal adenocarcinoma

The present study was conducted in collaboration with Laboratory of Tumor Microenvironment, Istituto di Ricerche Farmacologiche Mario Negri (Milan, Italy). For further details refer to appendix I, publication #4.

Pancreatic ductal adenocarcinoma (PDAC) is the most common neoplasia of the exocrine pancreas in humans, and its development is characterized by the evolution of normal pancreatic cells into hyperplastic, dysplastic and early neoplastic lesions (i.e. pancreatic intraepithelial neoplasia (PanIN)) towards the invasive carcinoma. PDAC epidemiology is characterized by rather low incidence (it is the 11th cancer by incidence) but high mortality: it represents the 4th cause of cancer-related death in the USA, with a 5-year survival rate of less than 5% [85].

At diagnosis, about 80% of the patients have already developed a metastatic disease (52% with distant metastasis to the liver or lungs). The late diagnosis is mostly attributable to the late development and not-specific clinical symptoms. In light of this, the development of early detection techniques to screen the population at risk is considered urgent and essential.

The aim of the present study was the identification of circulating biomarkers as an early detection method for PDAC. In the preliminary phase of this study, performed by Laboratory of Tumor Microenvironment (Istituto Mario Negri, Milan), a cohort of 131 human patients and matched controls was screened, to identify candidate molecules as biomarkers of PDACs [86]. Of the 7 molecules that has been identified in the preliminary phase, 3 were selected and further investigated in an experimental setting, which allowed to reproduce the early stages of development of the disease. The investigated molecules were:

- Matrix metalloproteinasis-7 (MMP-7): is a zinc-dependent endopeptidasis. Unlike other MMPs which are mainly stromal proteins, MMP-7 is mainly expressed on epithelial cells of glandular tissues and related lesions and involved in the cell surface proteolysis. In the pancreatic tissue, it has been recognized as an inducer of acinar-ductal metaplasia and to have a role in the regulation of apoptosis.
- Tissue inhibitor of metalloproteinasis-1 (TIMP-1): TIMP1 is an inhibitor of MMPs, involved in the regulation of extracellular matrix deposition and stroma remodeling, influencing the process of tumor development and metastatic spread. Beside MMPs inhibitory activity, TIMP-1 has also been shown to independently influence carcinogenesis by activating pro-survival signaling and inhibiting apoptosis.
- Thrombospondin-2 (THBS-2): is a homotrimeric glycoprotein that mediates cell-to-cell and cell-to-matrix interactions. It is a well-known inhibitor of angiogenesis in diverse settings, including tumors, but its role in carcinogenesis is controversial.

The aim of the present preclinical study was to validate a subset of the previously identified circulating biomarkers in preclinical experimental models of PDAC. For that purpose, two different mouse models were chosen:

- KC genetically engineered mouse -previously described in the literature [87]- was used to investigate the early phases of the development of the disease (PanIN).

- 3 patient-derived xenografts (PDXs) were established, characterized and used to investigate later stages in which tumors are full-developed.

EXPERIMENT I – CHARACTERIZATION OF PDXS

Materials and methods

In vivo experiment. The first part of the project was aimed at characterizing the three in-house established PDAC-PDXs models. For that purpose, each tumor was engrafted into immunocompromised mice (nude or SCID mice), either in the subcutaneous tissue or in an orthotopic site (intrapancreas transplant) and expanded up to 5 subsequent generations. Subcutaneous and pancreatic masses were collected and frozen for molecular assays and routinely processed for histopathological examination.

Histopathology. Histopathology was performed to evaluate the preservation of morphological features by comparing the respective patient's tumor (p0) with early (p1-p2) and late (p4-p5) passages of the xenografts in the mouse, collected from two different implantation sites (subcutis and pancreas). Further characterization was performed by quantification of desmoplasia with Sirius red histochemical stain for collagen (see appendix V) and by immunohistochemistry with species-specific markers (tab. 3.1), to assess the origin of the different components of the tumor.

TABLE 3.1 – List of primary antibodies used for PDXs characterization (see appendix III and IV for details).

Antibody	Specificity
Human MHC I	Cells of human origin
Vimentin sp20	Mesenchymal cells of human origin
Vimentin EPR3776	Mesenchymal cells of human and murine origin

Results

Orthotopic engraftment demonstrated to better reproduce the patient's tumor, compared to the subcutaneous route. Indeed, patients' primary tumors and mouse intrapancreatic xenografts were characterized by an expansile and multifocally infiltrative neoplastic proliferation, in which neoplastic cells were mainly arranged into tubules, surrounded and infiltrated by a large amount of desmoplastic tissue (fig. 3.1 A and B). On the contrary, subcutaneous xenografts, were composed of an expansile mass, with a cysto-papillary architecture, with abundant central necrosis and a drastically reduced amount of tumor-infiltrating stroma (fig. 3.1 C), as demonstrated also by Sirius red staining (fig. 3.2). Immunohistochemistry with antibodies listed in table 3.1 allowed to confirm the expected human origin of neoplastic cells and the host-derivation of the stromal components. Morphological features and molecular profile (data not shown) of the patient's tumor were maintained over several passages in the mouse.
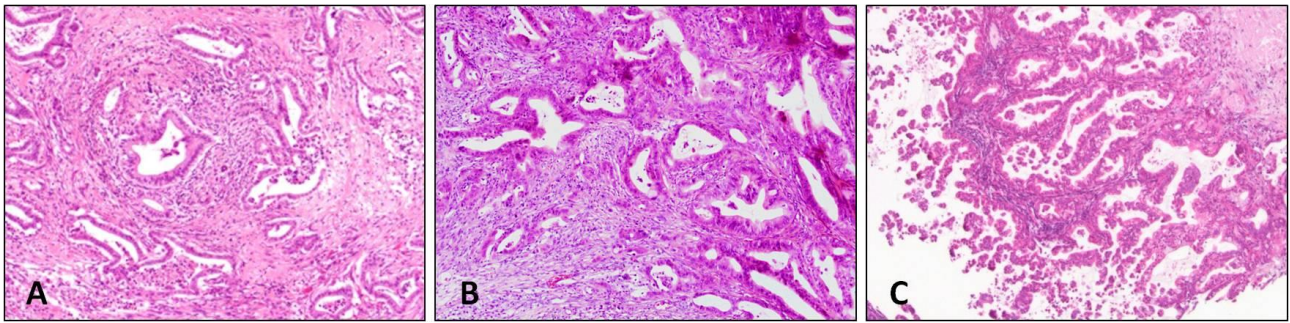
FIGURE 3.1 – Comparison between patient's tumor (A), orthotopic xenograft (B) and subcutaneous xenograft (C). H&E, 100x magnification.
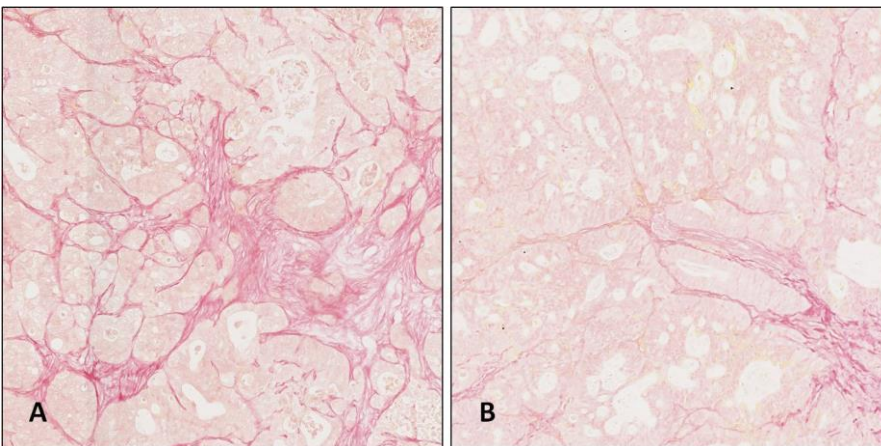
FIGURE 3.2 – Comparison between the amount of desmoplasia in the orthotopic xenograft (A) and subcutaneous xenograft (B). Sirius red staining, 100x magnification.

Conclusions

As the orthotopic route allows to better reproduce the patient's tumor, intrapancreas engraftment was chosen for the following experiment.

EXPERIMENT II – PRECLINICAL VALIDATION OF 3 PREVIOUSLY IDENTIFIED BIOMARKERS
Materials and methods

KC mice were monitored for 330 days. In PDX bearing mice, tumoral growth was monitored by magnetic resonance. The plasmatic concentration of the 3 selected biomarkers (TIMP1, MMP7 and THBS2) were measured with an ELISA kit at regular intervals during the development of the disease in both models. At sacrifice, the pancreas was collected and routinely processed for histopathological analysis. Immunohistochemistry for the 3 selected biomarkers was performed with the antibodies listed in table 3.2

Statistics. Differences in plasma concentration of the 3 biomarkers, between the different timepoints or between each group and the related control, were analyzed by the Mann-Whitney non-parametric test. Differences were considered significant when $p < 0.05$.

TABLE 3.2 – List of primary antibodies used for biomarkers validation (see appendix III and IV for details).

Antibody	Specificity
TIMP1	Human and murine TIMP1
MMP7	Murine MMP7
THBS2	Human and murine THBS2

Results

At sacrifice, KC mice presented different stages of PanIN progression (PanIN1A, PanIN1B and PanIN2). All the PDXs-bearing mice presented a tumoral mass which replaced and occasionally infiltrated the pancreas. In KC mice, a progressive increase of the plasmatic concentrations of the 3 biomarkers was observed over the time (fig. 3.3 A); at sacrifice, the increase was significantly different from control mice (healthy controls and PdxCre) and from mice with cerulein-induced chronic pancreatitis (fig. 3.3 B). The same finding was observed in PDXs-bearing mice which had higher plasmatic concentrations of MMP7, TIMP1 and THBS2 compared to the healthy controls (fig. 3.3 C).
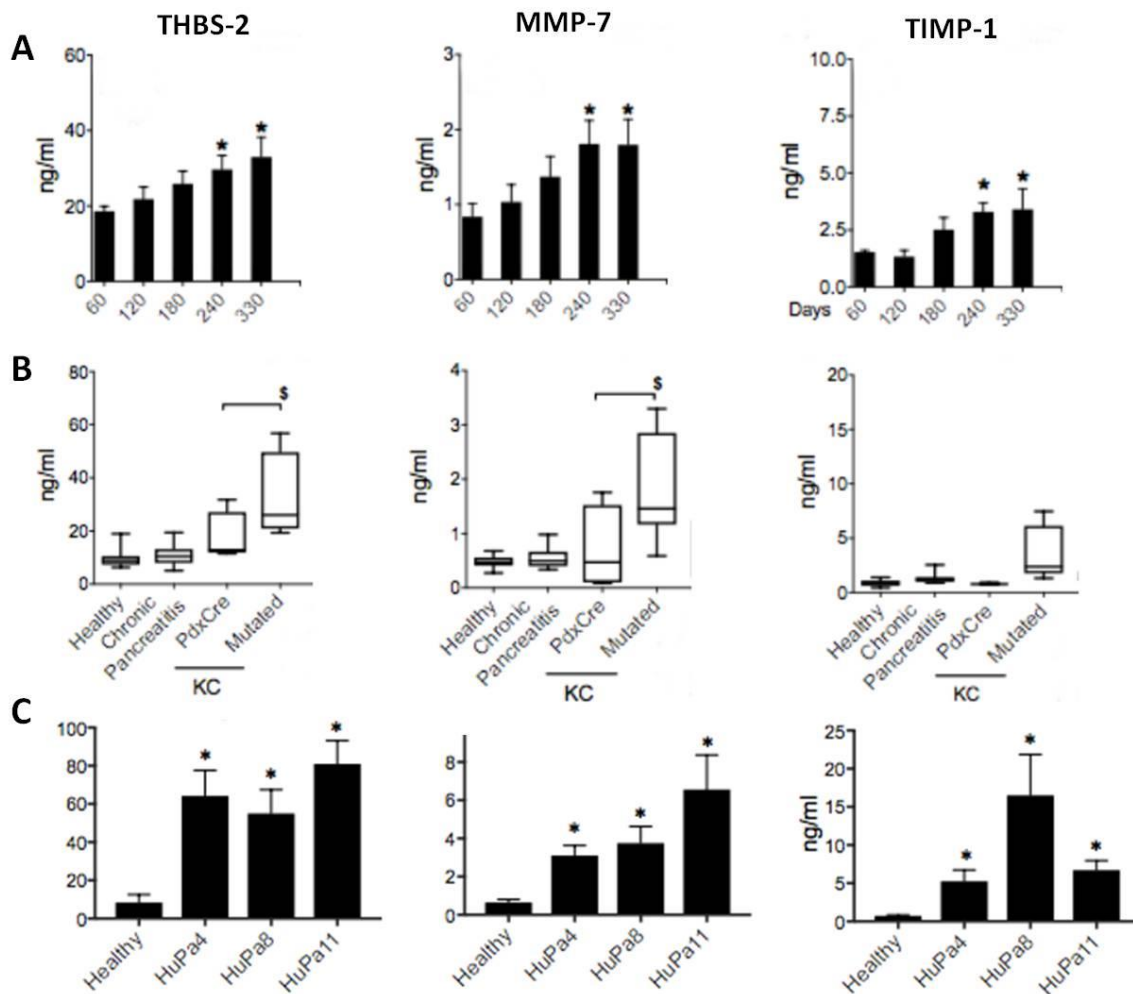
FIGURE 3.3 – Plasmatic concentration of the 3 biomarkers. A) KC model, concentration at different time point. B) plasmatic concentration at sacrifice compared to related controls. C) PDXs models, plasmatic concentrations at sacrifice. Modified from Resovi et al., 2018 [86].

In immunostained slides, MMP7 was mainly expressed by epithelial cells in PanIN lesions, and by normal duct cells in a milder way. THBS2 and TIMP1 immunoreactivity was observed in the stroma surrounding PanIN lesions with an increase expression along with progression of the disease (fig. 3.4). In PDXs models, any MMP7 immunoreactivity was observed, due to the mouse specificity of the primary antibody used (not reactive with human MMP7 protein). On the contrary, TIMP1 and THBS2 were mainly expressed on tumoral stroma, with a tumor-related variability (fig. 3.5).
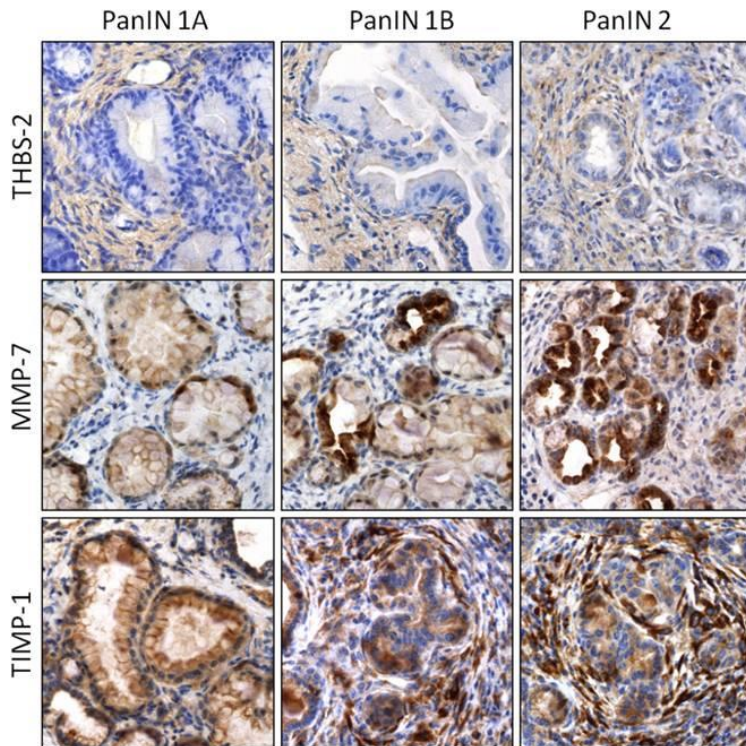
FIGURE 3.4 – Immunohistochemical expression of THBS-2, MMP-7 and TIMP-1 in different stages of PanIN progression. 200x magnification.
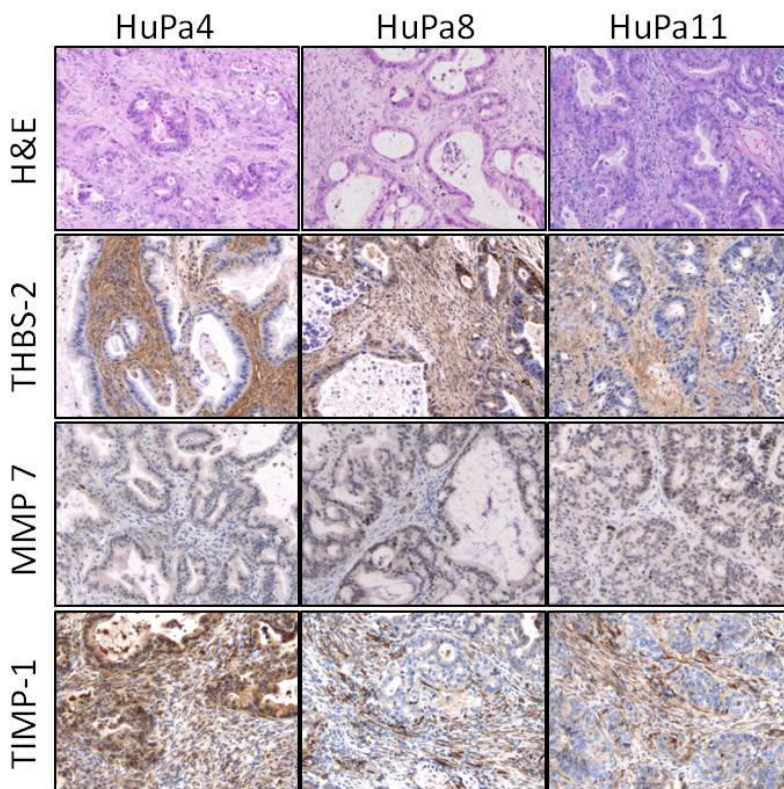
FIGURE 3.5 – H&E and immunohistochemical expression of THBS-2, MMP-7 and TIMP-1 in the 3 different PDXs. 200x magnification.

Conclusions

The 3 investigated circulating molecules represent promising biomarkers for the early detection of PDAC and accordingly, further investigation in a clinical trial on human patients is desirable. By

immunohistochemical analysis we were able to demonstrate that both tumoral cells and associated stroma play a role in the production and release of such biomarkers.

STUDY VIII – Hyaluronidase treatment improves tissue biodistribution of chemotherapeutic drugs

The present study was conducted in collaboration with Laboratory of Cancer Pharmacology, Istituto di Ricerche Farmacologiche Mario Negri (Milan, Italy).

Hyaluronic acid (HA) is a glycosaminoglycan polymer and one of the major components of the connective tissue extracellular matrix. The role of HA in tumors has been extensively investigated and accumulation of HA has been reported in a wide variety of human tumors and often correlated with high tumor grade, local and distant invasion and poor outcome [88]. Beside the previously described ability of HA together with the other components of the ECM to retain cytokines and growth factors, the role of HA in the TME is also related to its property to bind large amount of water, thus increasing interstitial fluid pressure. Increased interstitial fluid pressure has been linked to compression of tumor vasculature, poor tissue perfusion and therefore reduced delivery of systemically administered therapeutic drugs [89,90].

Matrix-assisted laser desorption/ionization mass spectrometry imaging (MALDI MSI) is a technique, widely used in pharmacological research, that allows to evaluate the spatial distribution and quantify macromolecules (including some therapeutic compounds), based on their mass, within an *ex vivo* collected tissue [91,92].

The aim of the present study was to evaluate the influence of hyaluronidase administration in the composition of tumoral stroma and in tumor biodistribution of the co-administered chemotherapeutic compound.

Materials and Methods

In vivo experiment. Two different experiments (Experiment I and Experiment II) with similar study design were performed: tumoral models (tab.3.3) of human origin were subcutaneously engrafted in 6- to 7-week-old female NCr-*nu/nu* mice mice. Mice were treated with paclitaxel (control group) or paclitaxel in combination with hyaluronidase (combination group). Mice were sacrificed at 4 h after last dose of PTX and subcutaneous tumors were immediately snap frozen in liquid nitrogen and stored at -80°C. 7 µm-thick serial sections from each sample were cut at the cryostat. For each sample, one section was analyzed with MALDI-MSI technique and serial sections used for histopathology.

TABLE 3.3 – Tumoral models.

Model	Description
SKOV3	Ovarian carcinoma cell line of human origin.
SKOV-HAS3	Variant of SKOV3 cell line, overexpressing hyaluronic acid.
HOC-PDX	Ovarian carcinoma patient-derived xenograft.
PDAC-PDX	Pancreatic ductal adenocarcinoma cell line of human origin.

Histopathology. Slides were fixed in 10% neutral buffered formalin and routinely stained with Hematoxylin and Eosin and with Alcian blue pH 2.5 (see appendix VI), a histochemical stain for glycosaminoglycans and mucopolysaccharides. A general evaluation of morphological features of the tumors was performed and selected morphological parameters and the amount of Alcian blue positive staining was semiquantitative evaluated. Scoring system applied is reported in table 3.4.

Histopathological evaluation was performed blinded (i.e. without knowledge of the tumor model and the treatment group).

The first experiment was performed on SKOV3 cell line and its variant SKOV-HAS3, which overexpresses hyaluronic acid. Thanks to the promising results obtained in the first experiment, the same experiment was performed on one ovarian carcinoma patient-derived xenograft and one pancreatic ductal adenocarcinoma cell line (experiment II).

TABLE 3.4 – Scoring system for the evaluation of hyaluronic acid (Alcian blue staining).

Score	Description
-	Negative staining
+	Rare and limited areas positively stained
++	Multifocal areas positively stained (less than 50% of the evaluated fields)
+++	Diffuse stain (more than 50% of the fields)

Results

EXPERIMENT I

In experiment I SKOV3 cell line and its variant SKOV-HAS3, which overexpresses hyaluronic acid, were evaluated.

Tumoral masses were composed of extensive solid areas of undifferentiated neoplastic cells, arranged in lobules, infiltrated by a moderate to large amount of thin fibrovascular stroma and occasionally thicker fibrous septa. Occasionally in some tumors, loose tissue arrangement was observed and semiquantitatively scored (tab. 3.5). In general, control tumors from the SKOV3 cell line were characterized by a more compact structure with more defined lobules, compared with SKOV-HAS3 control tumors (fig. 3.6). Variably extended areas of necrosis were present throughout the neoplastic tissue with any correlation with tumor cell line or treatment group (tab. 3.5). Stromal Alcian blue staining was diffusely observed in SKOV-HAS3 paclitaxel-treated tumors but strongly reduced after hyaluronidase treatment (tab 3.5 and Fig. 3.7).
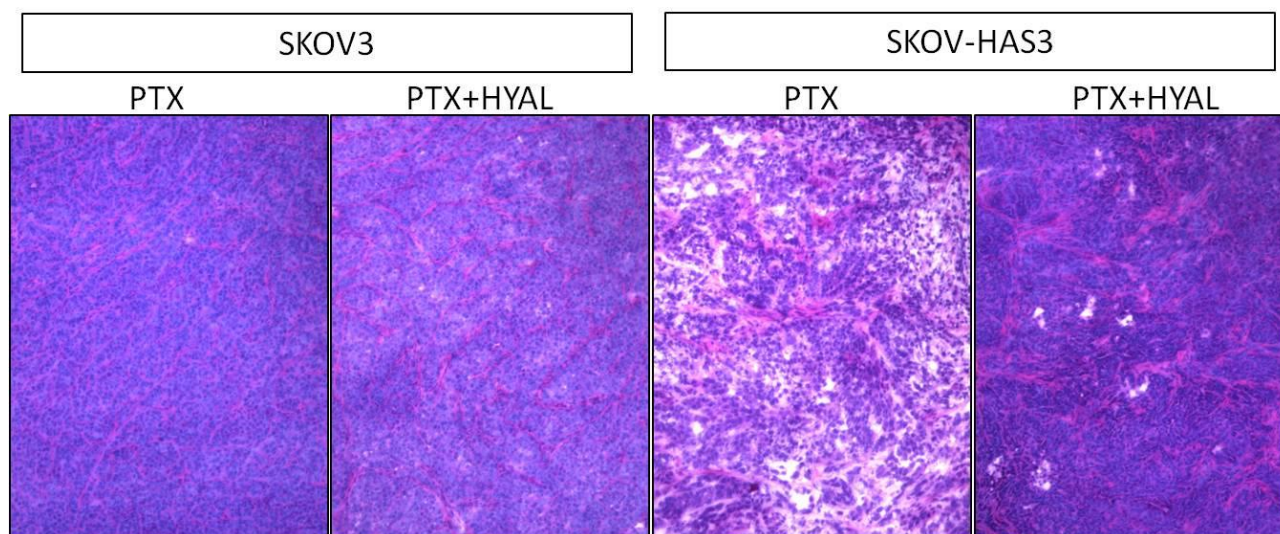
FIGURE 3.6 –SKOV-HAS3 control (PTX-treated) tumors are characterized by a more loosely arrangement of the tissue compared to SKOV3 tumors. Compact tissue architecture is restored after hyaluronidase treatment. H&E, 100x.

TABLE 3.5 – Semiquantitative analysis of morphological parameters and Alcian blue staining of SKOV3 and SKOV-HAS3 cell lines.

Group	Sample	Loose tissue arrangement	Alcian blue staining
SKOV 3			
PTX	#1	-	-
PTX	#2	-	Not evaluable
PTX	#3	-	-
PTX	#4	-	-
PTX+HYAL	#5	-	-
PTX+HYAL	#6	-	-
PTX+HYAL	#7	-	-
PTX+HYAL	#8	-	-
SKOV-HAS3			
PTX	#1	+++	+++
PTX	#2	++	+++
PTX	#3	++	+++
PTX+HYAL	#4	-	+
PTX+HYAL	#5	-	-
PTX+HYAL	#6	+	+
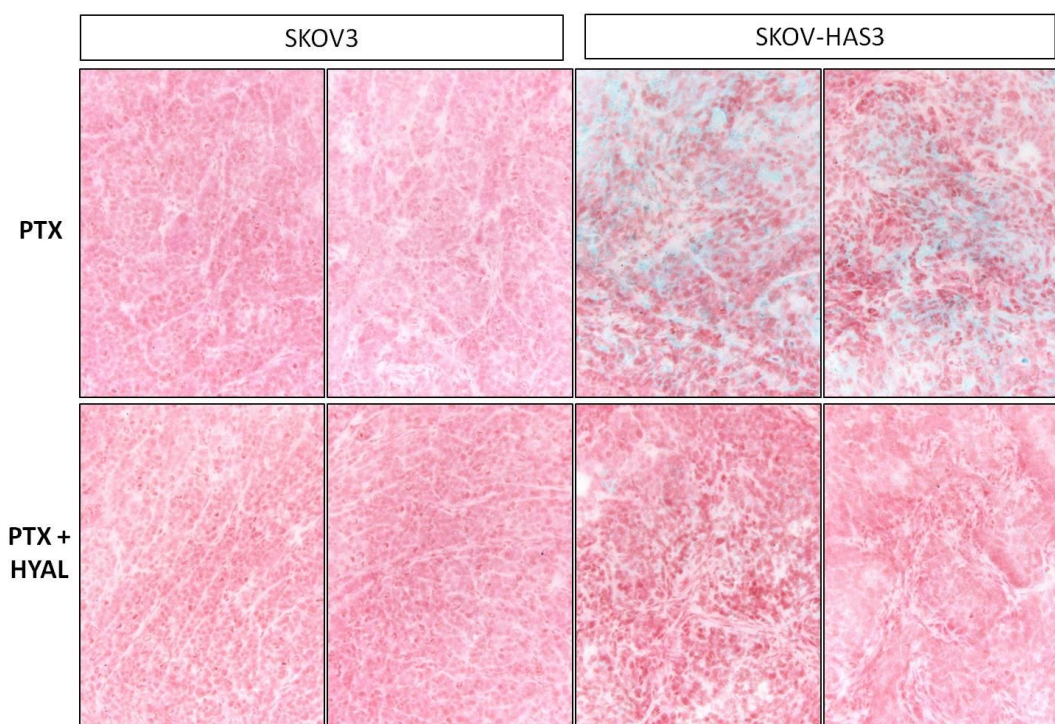
FIGURE 3.7 – Representative images from the 2 different cells lines and treatment groups. SKOV3 tumors (left) did not show Alcian blue positivity, independently from the treatment. SKOV-HAS3 control tumors (PTX groups) show marked Alcian blue stromal positivity, almost completely abolished by PTX+HYAL treatment. Alcian blue stain with nuclear red counterstain, 200x magnification.
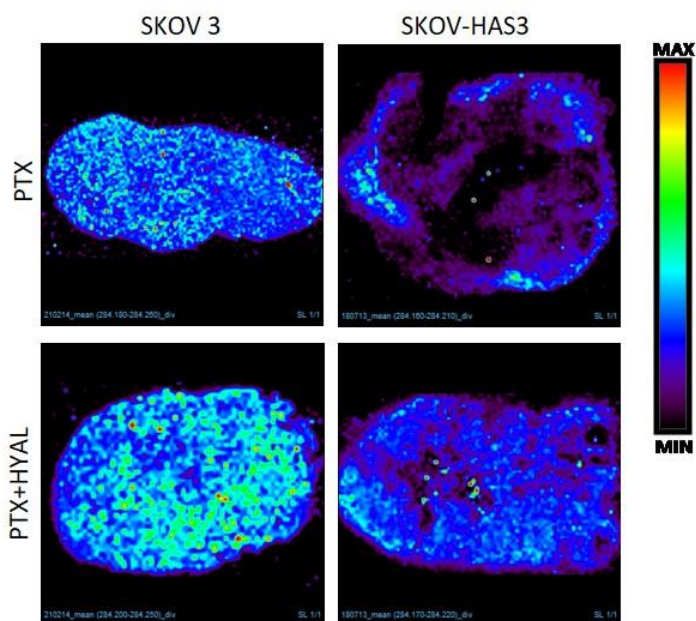
FIGURE 3.8 – Representative images of sections analysed with MALDI technique showing increased and more homogeneous distribution of PTX particularly in SKOV-HAS3 tumors.

EXPERIMENT II

In experiment II, experiment I was reproduced on two different tumor models, one ovarian carcinoma PDX and one pancreatic ductal adenocarcinoma cell line.

HOC-PDX tumoral masses were composed of densely cellular sheets/solid areas of undifferentiated neoplastic cells, with occasional formation of tubular structures and infiltrated by a minimal collagenous stroma. Alcian blue staining was multifocally to diffusely distributed in the stroma of HOC-PDX samples, with variable staining intensity. BxPC3 tumoral cells were arranged in solid areas and tubules dissected by thick fibrovascular septa (desmoplasia). Tubular lumina and lining epithelium were frequently filled with amorphous amphophilic material (mucins) which stained positive with Alcian blue. In Alcian blue stained slides, for the semiquantitative evaluation of hyaluronic acid, only interstitial positivity was considered, while extracellular accumulation of Alcian blue positive material (mucin lakes), intratubular as well as intracellular material were considered as mucins.

Hyaluronidase treatment extensively reduced the Alcian blue positive interstitium in both models, and in particular in HOC-PDX (tab 3.6 and 3.7 and figs 3.9 and 3.10). Similarly to experiment I, tissutal distribution of paclitaxel was improved by the combination treatment in both tumoral models even if the effect is not striking as in ovarian model (fig. 3.11).

TABLE 3.6 – Semiquantitative analysis of morphological parameters and Alcian blue staining of HOC-PDX.

Group	Sample	Loose tissue arrangement	Alcian blue staining
PTX	#1	+	+++
PTX	#2	+	+++
PTX	#3	+	++
PTX+HYAL	#4	-	-
PTX+HYAL	#5	-	-
PTX+HYAL	#6	+	+

TABLE 3.7 – Semiquantitative analysis of morphological parameters and Alcian blue staining of BxPC3.

Group	Sample	Loose tissue arrangement	Alcian blue staining
PTX	#1	-	++
PTX	#2	-	++
PTX	#3	-	+
PTX+HYAL	#4	-	+
PTX+HYAL	#5	-	+
PTX+HYAL	#6	-	+
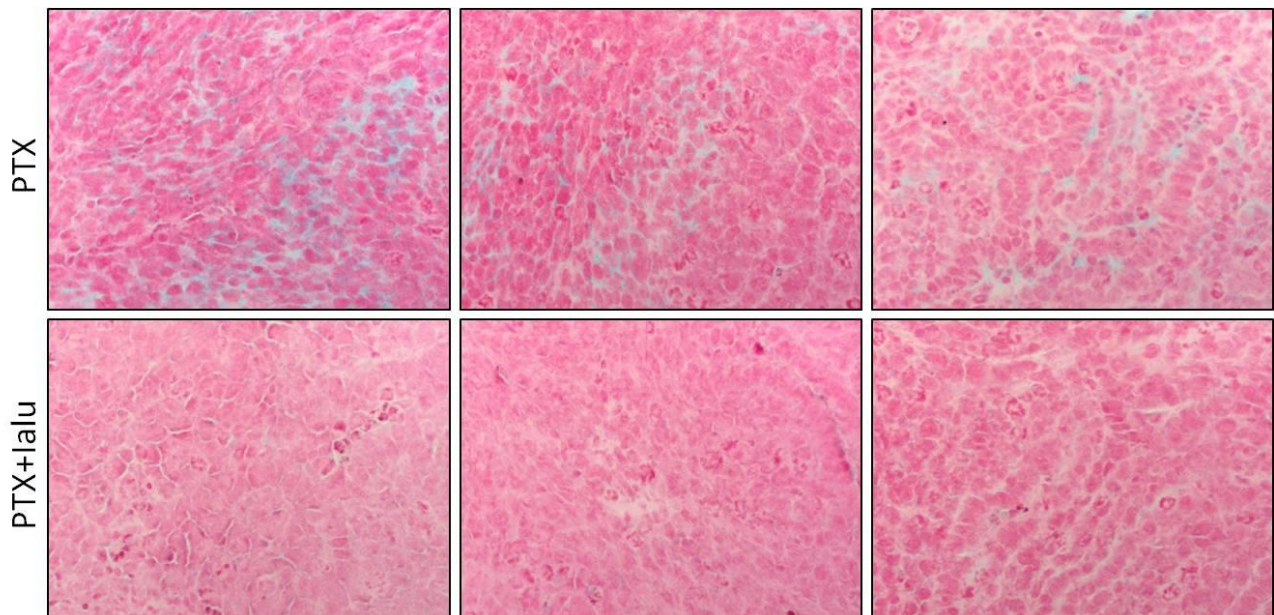
FIGURE 3.9 – Representative microscopic fields from HOC-PDX tumors. Alcian blue stain with nuclear red counterstain, 400x magnification.
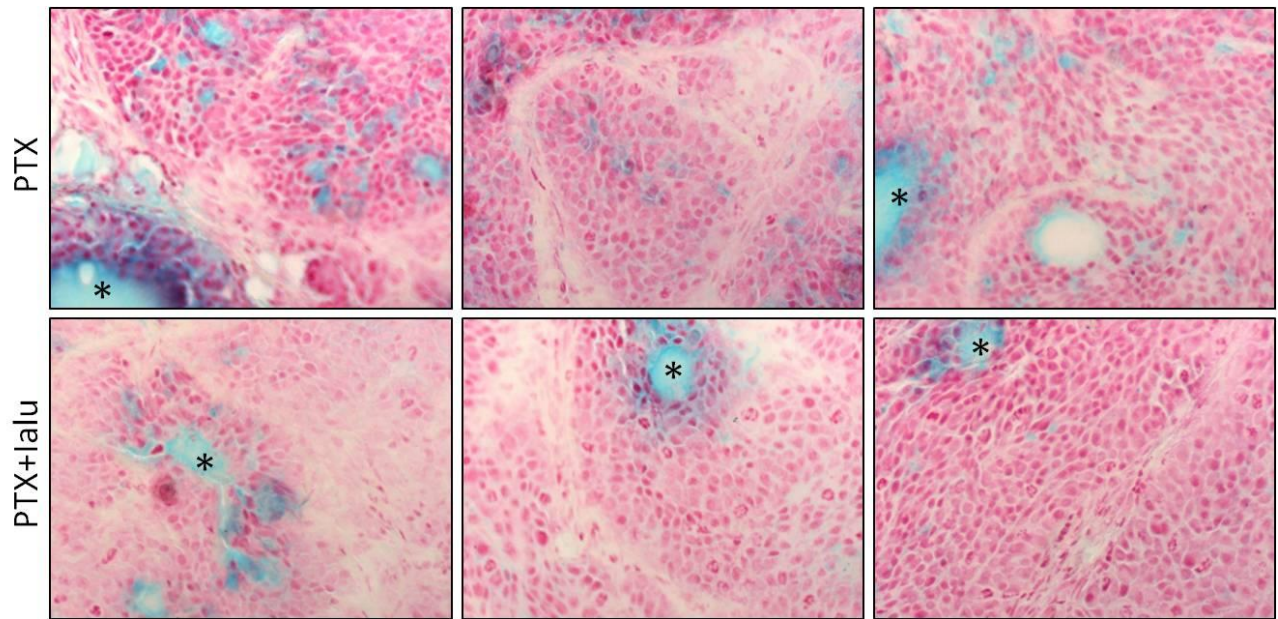
FIGURE 3.10 – Representative microscopic fields from BxPC3 tumors. Alcian blue stain with nuclear red counterstain, 400x magnification. *Mucin lakes.
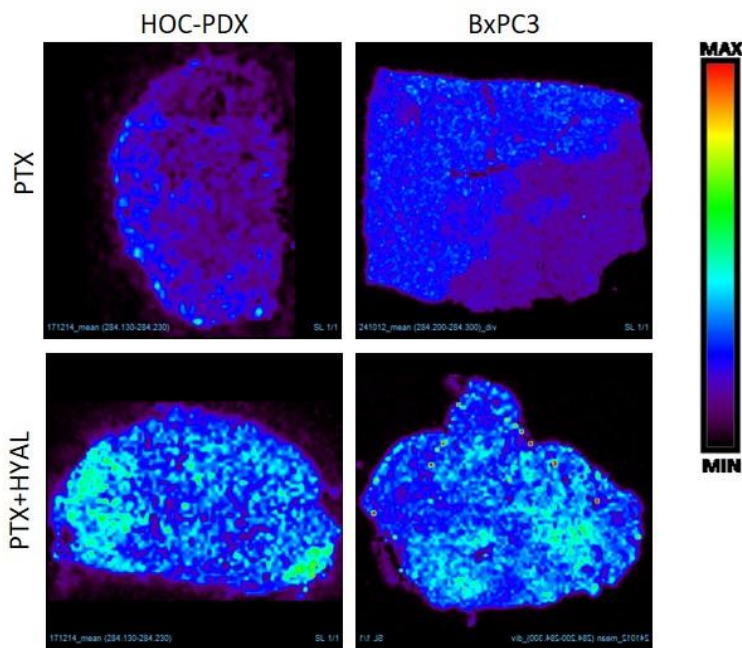
FIGURE 3.11 – Representative images of sections analysed with MALDI technique showing increased and more homogeneous distribution of PTX in the tumor tissue of both tumoral models.

Conclusions

Hyaluronic acid is one of the major components of the connective tissue extracellular matrix and is known to play a pivotal role in the maintenance of stromal architecture also in tumoral settings. However its ability to bind large amount of water molecules could be responsible for the more loosely arrangement of the tumoral tissue observed in SKOV-HAS3 and to a lesser extent in HOC-PDX samples: high amount of water are thus frozen and released during sample preparation for cryostatic sectioning, producing the observed artifacts characterized by clear/empty spaces which dissect the tumoral tissue.

Histopathological evaluation of tumor samples and in particular with Alcian blue histochemical stain, confirmed the HA-depleting activity of hyaluronidase. This result was particularly evident in SKOV-HAS3 and HOC-PDX tumoral models, which were characterized by marked basal expression of HA.

Evaluation of tumor sections with MALDI imaging showed that co-administration of hyaluronidase with paclitaxel improved the biodistribution of the chemotherapeutic compound within the tumoral tissue, which, in SKOV-HAS3 tumors, resulted in a delayed tumoral growth (data not shown).

References

1. Bray F, Ferlay J, Soerjomataram I, Siegel RL, Torre LA, Jemal A. Global cancer statistics 2018: GLOBOCAN estimates of incidence and mortality worldwide for 36 cancers in 185 countries. *CA Cancer J Clin.* 2018;68(6):394-424. doi:10.3322/caac.21492.

2. Workman P, Aboagye EO, Balkwill F, et al. Guidelines for the welfare and use of animals in cancer research. *Br J Cancer.* 2010;102(11):1555-1577. doi:10.1038/sj.bjc.6605642.

3. Carmeliet P, Jain RK. Molecular Mechanisms and and clinical applications of angiogenesis. *Nature.* 2011;473(7347):298-307. doi:10.1038/nature10144.Molecular.

4. Hanahan D, Weinberg RA. Hallmarks of cancer: The next generation. *Cell.* 2011;144(5):646-674. doi:10.1016/j.cell.2011.02.013.

5. Carmeliet P. Angiogenesis in Health and Disease : Therapeutic Opportunities. *Nat Med.* 2003;9(6):653-660.

6. Jain RK. Normalization of tumor vasculature: an emerging concept in antiangiogenic therapy. *Science.* 2005;307(5706):58-62. doi:10.1126/science.1104819.

7. Hashizume H, Baluk P, Morikawa S, et al. Openings between defective endothelial cells explain tumor vessel leakiness. *Am J Pathol.* 2000;156(4):1363-1380. doi:10.1016/S0002-9440(10)65006-7.

8. Morikawa S, Baluk P, Kaidoh T, Haskell A, Jain RK, McDonald DM. Abnormalities in pericytes on blood vessels and endothelial sprouts in tumors. *Am J Pathol.* 2002;160(3):985-1000. doi:10.1016/S0002-9440(10)64920-6.

9. Baluk P, Morikawa S, Haskell A, Mancuso M, McDonald DM. Abnormalities of basement membrane on blood vessels and endothelial sprouts in tumors. *Am J Pathol.* 2003;163(5):1801-1815. doi:10.1016/S0002-9440(10)63540-7.

10. Maniotis A, Folberg R, Hess A, et al. Vascular channel formation by human melanoma cells in vivo and in vitro: vasculogenic mimicry. *Am J Pathol.* 1999;155(3):739-752. doi:10.1016/S0002-9440(10)65173-5.

11. Ge H, Luo H. Overview of advances in vasculogenic mimicry - a potential target for tumor therapy. *Cancer Manag Res.* 2018;10:2429-2437. doi:10.2147/CMAR.S164675.

12. McDonald DM, Choyke PL. Imaging of angiogenesis: from microscope to clinic. *Nat Med.* 2003;9(6):713-725. doi:10.1038/nm0603-713.

13. Hagendoorn J, Tong R, Fukumura D, et al. Onset of abnormal blood and lymphatic vessel function and interstitial hypertension in early stages of carcinogenesis. *Cancer Res.* 2006;66(7):3360-3364. doi:10.1158/0008-5472.CAN-05-2655.

14. El-Kenawi AE, El-Remessy AB. Angiogenesis inhibitors in cancer therapy: Mechanistic perspective on classification and treatment rationales. *Br J Pharmacol.* 2013;170(4):712-729. doi:10.1111/bph.12344.

15. Jain RK. Antiangiogenesis Strategies Revisited: From Starving Tumors to Alleviating Hypoxia. *Cancer Cell.* 2014;26(5):605-622. doi:10.1016/j.ccell.2014.10.006.

16. Vaupel P, Mayer A. Hypoxia in cancer: significance and impact on clinical outcome. *Cancer Metastasis Rev.* 2007;26(2):225-239. doi:10.1007/s10555-007-9055-1.

17. Multhoff G, Radons J, Vaupel P. Critical role of aberrant angiogenesis in the development of tumor hypoxia and associated radioresistance. *Cancers (Basel).* 2014;6(2):813-828. doi:10.3390/cancers6020813.

18. Das V, Štěpánková J, Hajdúch M, Miller JH. Role of tumor hypoxia in acquisition of resistance to microtubule-stabilizing drugs. *Biochim Biophys Acta - Rev Cancer.* 2015;1855(2):172-182. doi:10.1016/J.BBCAN.2015.02.001.

19. Bayer C, Vaupel P. Acute versus chronic hypoxia in tumors. *Strahlentherapie und Onkol.* 2012;188(7):616-627. doi:10.1007/s00066-012-0085-4.

20. Bayer C, Shi K, Astner ST, Maftei C-A, Vaupel P. Acute versus chronic hypoxia: why a simplified classification is simply not enough. *Int J Radiat Oncol Biol Phys.* 2011;80(4):965-968. doi:10.1016/j.ijrobp.2011.02.049.

21. Zeng W, Liu P, Pan W, Wei Y. Hypoxia and hypoxia inducible factors in tumor metabolism. *Cancer Lett.* 2015;356(2):263-267. doi:10.1016/j.canlet.2014.01.032.

22. Ruan K, Song G, Ouyang G. Role of hypoxia in the hallmarks of human cancer. *J Cell Biochem.* 2009;107(6):1053-1062. doi:10.1002/jcb.22214.

23. Martin JD, Seano G, Jain RK. Normalizing Function of Tumor Vessels: Progress, Opportunities, and Challenges. 2019. doi:10.1146/annurev-physiol-020518.

24. Folkman J. Tumor Angiogenesis: Therapeutic Implications. *N Engl J Med.* 1971;285:1182–1186. doi:10.1056/NEJM197111182852108.

25. Yu JL, Kerbel RS, Coomber BL. A paradigm for therapy-induced microenvironmental changes in solid tumors leading to drug resistance. *Differentiation.* 2002;70(9-10):599-609. doi:10.1046/J.1432-0436.2002.700913.X.

26. Al-Abd AM, Alamoudi AJ, Abdel-Naim AB, Neamatallah TA, Ashour OM. Anti-angiogenic agents for the treatment of solid tumors: Potential pathways, therapy and current strategies - A review. *J Adv Res.* 2017;8(6):591-605. doi:10.1016/j.jare.2017.06.006.

27. Liu J, Matulonis UA. New strategies in ovarian cancer: Translating the molecular complexity of ovarian cancer into treatment advances. *Clin Cancer Res.* 2014;20(20):5150-5156. doi:10.1158/1078-0432.CCR-14-1312.

28. Hasan J, Byers R, Jayson G. Intra-tumoural microvessel density in human solid tumours. *Br J Cancer.* 2002;86:1566-1577. doi:10.1038/sj/bjc/6600315.

29. Sartori A, Corno C, De Cesare M, et al. Efficacy of a Selective Binder of αVβ3 Integrin Linked to the Tyrosine Kinase Inhibitor Sunitinib in Ovarian Carcinoma Preclinical Models. *Cancers (Basel).* 2019;11(4). doi:10.3390/cancers11040531.

30. E Ljungkvist AS, Bussink J, A M Kaanders JH, van der Kogel AJ, der Kogel V. Dynamics of Tumor Hypoxia Measured with Bioreductive Hypoxic Cell Markers. *Radiat Res Radiat Res.* 2007;167(167):127-145.

31. Gulliksrud K, Vestvik IK, Galappathi K, Mathiesen B, Rofstad EK. Detection of Different Hypoxic Cell Subpopulations in Human Melanoma Xenografts by Pimonidazole Immunohistochemistry. *Radiat Res.* 2008;170(5):638-650. doi:10.1667/RR1400.1.

32. D'Angelo E, Prat J. Classification of ovarian carcinomas based on pathology and molecular genetics. *Clin Transl Oncol.* 2010;12(12):783-787. doi:10.1007/s12094-010-0599-0.

33. Lim D, Oliva E. Precursors and pathogenesis of ovarian carcinoma. *Pathology.* 2013;45(3):229-242. doi:10.1097/PAT.0b013e32835f2264.

34. Lord CJ, Ashworth A. PARP inhibitors: Synthetic lethality in the clinic. *Science.* 2017;355(6330):1152-1158. doi:10.1126/science.aam7344.

35. Ringley JT, Moore DC, Patel J, Rose MS. Poly (ADP-ribose) Polymerase Inhibitors in the Management of Ovarian Cancer: A Drug Class Review. *P T.* 2018;43(9):549-556. http://www.ncbi.nlm.nih.gov/pubmed/30186027. Accessed September 9, 2018.

36. Taylor KN, Eskander RN. PARP Inhibitors in Epithelial Ovarian Cancer. *Recent Pat Anticancer Drug Discov.* 2018;13(2):145-158. doi:10.2174/1574892813666171204094822.

37. Kaplan AR, Gueble SE, Liu Y, et al. Cediranib suppresses homology-directed DNA repair through down-regulation of BRCA1/2 and RAD51. *Sci Transl Med.* 2019;11(492):eaav4508. doi:10.1126/scitranslmed.aav4508.

38. Ehrlich P. Ueber den jetzigen Stand der Karzinomforschung. *Ned Tijdschr Geneeskd.* 1909;5:273-290.

39. Schreiber RD, Old LJ, Smyth MJ. Cancer Immunoediting: Integrating Immunity's Roles in Cancer Suppression and Promotion. *Science (80-).* 2011;331(6024):1565-1570. doi:10.1126/science.1203486.

40. Shankaran V, Ikeda H, Bruce AT, et al. IFNγ and lymphocytes prevent primary tumour development and shape tumour immunogenicity. *Nature.* 2001;410(6832):1107-1111. doi:10.1038/35074122.

41. Vinay DS, Ryan EP, Pawelec G, et al. Immune evasion in cancer: Mechanistic basis and therapeutic strategies. *Semin Cancer Biol.* 2015;35:185-198. doi:10.1016/j.semcancer.2015.03.004.

42. Grivennikov SI, Greten FR, Karin M. Immunity, Inflammation, and Cancer. *Cell.* 2010;140(6):883-899. doi:10.1016/j.cell.2010.01.025.

43. Colotta F, Allavena P, Sica A, Garlanda C, Mantovani A. Cancer-related inflammation, the seventh hallmark of cancer: links to genetic instability. *Carcinogenesis.* 2009;30(7):1073-1081. doi:10.1093/carcin/bgp127.

44. Karin M. Nuclear factor-κB in cancer development and progression. *Nature.* 2006;441(7092):431-436. doi:10.1038/nature04870.

45. Grivennikov SI, Karin M. Dangerous liaisons: STAT3 and NF-κB collaboration and crosstalk in cancer. *Cytokine Growth Factor Rev.* 2010;21(1):11-19. doi:10.1016/J.CYTOGFR.2009.11.005.

46. Yu H, Pardoll D, Jove R. STATs in cancer inflammation and immunity: a leading role for STAT3. *Nat Rev Cancer.* 2009;9(11):798-809. doi:10.1038/nrc2734.

47. Lin L, Chen Y-S, Yao Y-D, et al. CCL18 from tumor-associated macrophages promotes angiogenesis in breast cancer. *Oncotarget.* 2015;6(33):34758-34773. doi:10.18632/oncotarget.5325.

48. Riabov V, Gudima A, Wang N, Mickley A, Orekhov A, Kzhyshkowska J. Role of tumor associated macrophages in tumor angiogenesis and lymphangiogenesis. *Front Physiol*. 2014;5:75. doi:10.3389/fphys.2014.00075.

49. Mantovani A, Sozzani S, Locati M, Allavena P, Sica A, Mantovani A. Macrophage polarization : tumor-associated macrophages as a paradigm for polarized M2 mononuclear phagocytes. 2002;23(11):549-555.

50. Mantovani A, Allavena P, Sica A, Balkwill F. Cancer-related inflammation. *Nature*. 2008;454(7203):436-444. doi:10.1038/nature07205.

51. Langers I, Renoux VM, Thiry M, Delvenne P, Jacobs N. Natural killer cells: role in local tumor growth and metastasis Introduction to natural killer cells in antitumor immune response. *Biol Targets Ther*. 2012;6:73-82. doi:10.2147/BTT.S23976.

52. Fridman WH, Pagès F, Sautès-Fridman C, Galon J. The immune contexture in human tumours: impact on clinical outcome. *Nat Rev Cancer*. 2012;12(4):298-306. doi:10.1038/nrc3245.

53. Tachibana T, Onodera H, Tsuruyama T, et al. Increased Intratumor V 24-Positive Natural Killer T Cells: A Prognostic Factor for Primary Colorectal Carcinomas. *Clin Cancer Res*. 2005;11(20):7322-7327. doi:10.1158/1078-0432.CCR-05-0877.

54. Galdiero MR, Bonavita E, Barajon I, Garlanda C, Mantovani A, Jaillon S. Tumor associated macrophages and neutrophils in cancer. *Immunobiology*. 2013;218(11):1402-1410. doi:10.1016/J.IMBIO.2013.06.003.

55. Chen DS, Mellman I. Oncology Meets Immunology: The Cancer-Immunity Cycle. *Immunity*. 2013;39(1):1-10. doi:10.1016/j.immuni.2013.07.012.

56. Motz GT, Coukos G. Deciphering and Reversing Tumor Immune Suppression. *Immunity*. 2013;39(1):61-73. doi:10.1016/J.IMMUNI.2013.07.005.

57. Velcheti V, Schalper K. Basic Overview of Current Immunotherapy Approaches in Cancer. *Am Soc Clin Oncol Educ book Am Soc Clin Oncol Annu Meet*. 2016;35(36):298-308. doi:10.1200/EDBK_156572.

58. Herzog CE. Overview of Sarcomas in the Adolescent and Young Adult Population. *J Pediatr Hematol Oncol*. 2005;27(4):215-218. https://ovidsp-dc2-ovid-com.pros.lib.unimi.it:2050/sp-4.02.0b/ovidweb.cgi?QS2=434f4e1a73d37e8c1c7f5031d0406d8c452eba8d0c8e891fc435b37f2d17486a7033270faa8ac6c96a2313efa7118b0f8ea02a646b093311c776036f872a5a624e770d2da6785ad3b478b877e310eaf51ff0302de7bd4d3b9.

59. Scheer M, Dantonello T, Hallmen E, et al. Synovial Sarcoma Recurrence in Children and Young Adults. *Ann Surg Oncol*. 2016;23(S5):618-626. doi:10.1245/s10434-016-5535-2.

60. Vlenterie M, Litière S, Rizzo E, et al. Outcome of chemotherapy in advanced synovial sarcoma patients: Review of 15 clinical trials from the European Organisation for Research and Treatment of Cancer Soft Tissue and Bone Sarcoma Group; setting a new landmark for studies in this entity. *Eur J Cancer*. 2016;58:62-72. doi:10.1016/J.EJCA.2016.02.002.

61. Friedrichs N, Küchler J, Endl E, et al. Insulin-like growth factor-1 receptor acts as a growth regulator in synovial sarcoma. *J Pathol*. 2008;216(4):428-439. doi:10.1002/path.2438.

62. Xie Y, Skytting B, Nilsson G, Brodin B, Larsson O. Expression of Insulin-like Growth Factor-1 Receptor in Synovial Sarcoma. *Cancer Res*. 1999;59(15).

http://www.ncbi.nlm.nih.gov/pubmed/9699666. Accessed August 29, 2019.

63.   Vlodavsky I, Singh P, Boyango I, et al. Heparanase: From basic research to therapeutic applications in cancer and inflammation. *Drug Resist Updat*. 2016;29:54-75. doi:10.1016/J.DRUP.2016.10.001.

64.   Cassinelli G, Dal Bo L, Favini E, et al. Supersulfated low-molecular weight heparin synergizes with IGF1R/IR inhibitor to suppress synovial sarcoma growth and metastases. *Cancer Lett*. 2018;415:187-197. doi:10.1016/J.CANLET.2017.12.009.

65.   Brennan T V., Lin L, Brandstadter JD, et al. Heparan sulfate mimetic PG545-mediated antilymphoma effects require TLR9-dependent NK cell activation. *J Clin Invest*. 2016;126(1):207-219. doi:10.1172/JCI76566.

66.   Qing W, Fang W-Y, Ye L, et al. Density of Tumor-Associated Macrophages Correlates with Lymph Node Metastasis in Papillary Thyroid Carcinoma. *Thyroid*. 2012;22(9):905-910. doi:10.1089/thy.2011.0452.

67.   Ryder M, Ghossein R, Ricarte-Filho J, Knauf J, Fagin J. Increased density of tumor-associated macrophages is associated with decreased survival in advanced thyroid cancer. *Endocr Relat Cancer*. 2008;15:1069-1074. https://erc.bioscientifica.com/view/journals/erc/15/4/1069.xml?rskey=prwZ7J&result=3. Accessed September 8, 2019.

68.   Mazzoni M, Mauro G, Erreni M, et al. Senescent thyrocytes and thyroid tumor cells induce M2-like macrophage polarization of human monocytes via a PGE2-dependent mechanism. *J Exp Clin Cancer Res*. 2019;38(1):208. doi:10.1186/s13046-019-1198-8.

69.   Rehg JE, Bush D, Ward JM. The Utility of Immunohistochemistry for the Identification of Hematopoietic and Lymphoid Cells in Normal Tissues and Interpretation of Proliferative and Inflammatory Lesions of Mice and Rats. *Toxicol Pathol*. 2012;40(2):345-374. doi:10.1177/0192623311430695.

70.   Chen ZW, Ahren B, Ostenson C, et al. Identification, isolation, and characterization of daintain (allograft inflammatory factor 1), a macrophage polypeptide with effects on insulin secretion and abundantly present in the pancreas of prediabetic BB rats. *Proc Natl Acad Sci U S A*. 1997;94(25):13879-13884. doi:10.1073/pnas.94.25.13879.

71.   Orsmark C, Skoog T, Jeskanen L, Kere J, Saarialho-Kere U. Expression of allograft inflammatory factor-1 in inflammatory skin disorders. *Acta Derm Venereol*. 2007;87(3):223-227. doi:10.2340/00015555-0225.

72.   International Agency for Research on Cancer. GLOBOCAN. Global Cancer Observatory.

73.   Terzić J, Grivennikov S, Karin E, Karin M. Inflammation and Colon Cancer. *Gastroenterology*. 2010;138(6):2101-2114. doi:10.1053/j.gastro.2010.01.058.

74.   Danussi C, Petrucco A, Wassermann B, et al. An EMILIN1-negative microenvironment promotes tumor cell proliferation and lymph node invasion. *Cancer Prev Res*. 2012;5(9):1131-1143. doi:10.1158/1940-6207.CAPR-12-0076-T.

75.   Thaker AI, Shaker A, Rao MS, Ciorba MA. Modeling colitis-associated cancer with azoxymethane (AOM) and dextran sulfate sodium (DSS). *J Vis Exp*. 2012;67(e4100):1-7. doi:10.3791/4100.

76.   Boivin GP, Washington K, Yang K, et al. Pathology of Mouse Models of Intestinal Cancer:

Consensus Report and Recommendations. *Gastroenterology*. 2003;124(3):762-777. doi:10.1053/gast.2003.50094.

77. Capuano A, Pivetta E, Sartori G, et al. Abrogation of EMILIN1-β1 integrin interaction promotes experimental colitis and colon carcinogenesis. *Matrix Biol*. August 2019. doi:10.1016/J.MATBIO.2019.08.006.

78. Perše M, Cerar A. Dextran Sodium Sulphate Colitis Mouse Model: Traps and Tricks. *J Biomed Biotechnol*. 2012;2012:1-13. doi:10.1155/2012/718617.

79. Dvorak HF. Tumors: Wounds That Do Not Heal. Similarities between tumor stroma generation and wound healing. *N Engl J Med*. 1986;315(26):1650-1659. doi:10.1056/NEJM198612253152606.

80. Kalluri R. The biology and function of fibroblasts in cancer. *Nat Rev Cancer*. 2016;16(9):582-598. doi:10.1038/nrc.2016.73.

81. Hynes RO, Naba A. Overview of the matrisome--an inventory of extracellular matrix constituents and functions. *Cold Spring Harb Perspect Biol*. 2012;4(1):a004903. doi:10.1101/cshperspect.a004903.

82. Bonnans C, Chou J, Werb Z. Remodelling the extracellular matrix in development and disease. *Nat Rev Mol Cell Biol*. 2014;15(12):786-801. doi:10.1038/nrm3904.

83. Flaberg E, Markasz L, Petranyi G, et al. High-throughput live-cell imaging reveals differential inhibition of tumor cell proliferation by human fibroblasts. *Int J Cancer*. 2011;128(12):2793-2802. doi:10.1002/ijc.25612.

84. Lochter A, Galosy S, Muschler J, Freedman N, Werb Z, Bissell MJ. Matrix metalloproteinase stromelysin-1 triggers a cascade of molecular alterations that leads to stable epithelial-to-mesenchymal conversion and a premalignant phenotype in mammary epithelial cells. *J Cell Biol*. 1997;139(7):1861-1872. doi:10.1083/jcb.139.7.1861.

85. Ilic M, Ilic I. Epidemiology of pancreatic cancer. *World J Gastroenterol*. 2016;22(44):9694-9705. doi:10.3748/wjg.v22.i44.9694.

86. Resovi A, Bani MR, Porcu L, et al. Soluble stroma-related biomarkers of pancreatic cancer. *EMBO Mol Med*. 2018;10(8). doi:10.15252/emmm.201708741.

87. Hingorani SR, Petricoin EF, Maitra A, et al. Preinvasive and invasive ductal pancreatic cancer and its early detection in the mouse. *Cancer Cell*. 2003;4(6):437-450. doi:10.1016/S1535-6108(03)00309-X.

88. Tammi R, Kultti A, Kosma, V Pirinen R, Auvinen P, Tammi M. Hyaluronan in human tumors: Pathobiological and prognostic messages from cell-associated and stromal hyaluronan. *Semin Cancer Biol*. 2008;18(4):288-295. doi:10.1016/J.SEMCANCER.2008.03.005.

89. Jacobetz MA, Chan DS, Neesse A, et al. Hyaluronan impairs vascular function and drug delivery in a mouse model of pancreatic cancer. *Gut*. 2013;62(1):112-120. doi:10.1136/gutjnl-2012-302529.

90. Minchinton AI, Tannock IF. Drug penetration in solid tumours. *Nat Rev Cancer*. 2006;6(8):583-592. doi:10.1038/nrc1893.

91. Cobice D, Goodwin R, Andren P, Nilsson A, Mackay C, Andrew R. Future technology insight: mass spectrometry imaging as a tool in drug research and development. *Br J*

Pharmacol. 2015;172:3266-3283.
https://bpspubs.onlinelibrary.wiley.com/doi/pdf/10.1111/bph.13135. Accessed September 18, 2019.

92.   Giordano S, Zucchetti M, Decio A, et al. Heterogeneity of paclitaxel distribution in different tumor models assessed by MALDI mass spectrometry imaging. *Sci Rep.* 2016;6:39284. doi:10.1038/srep39284.

Appendices

Appendix I – List of the scientific publications of the author included in this work

1. Sartori A, Corno C, De Cesare M, Scanziani E, **Minoli L**, Battistini L, Zanardi F, Perego P (2019). Efficacy of a Selective Binder of αVβ3 Integrin Linked to the Tyrosine Kinase Inhibitor Sunitinib in Ovarian Carcinoma Preclinical Models. *Cancers,*11(4).
2. Cassinelli G., Dal Bo L., Favini E., Cominetti D., Pozzi S., Tortoreto M., De Cesare M., Lecis D., Scanziani E., **Minoli L.**, Naggi, A., Vlodavsky I., Zaffaroni N., Lanzi C. (2018). Supersulfated low-molecular weight heparin synergizes with IGF1R/IR inhibitor to suppress synovial sarcoma growth and metastases. *Cancer letters*, 415, 187-197.
3. Capuano A, Pivetta E, Sartori G, Bosisio G, Favero A, Cover E, Andreuzzi E, Colombatti A, Cannizzaro R, Scanziani E, **Minoli L**, Bucciotti F, Lopez A, Gaspardo K, Doliana R, Mongiat M, Spessotto P (2019). Abrogation of EMILIN1-β1 integrin interaction promotes experimental colitis and colon carcinogenesis. *Matrix Biol*, Epub ahed of print.
4. Resovi A, Bani M, Porcu L, Anastasia A, **Minoli L**, Allavena P, Cappello P, Novelli F, Scarpa A, Morandi E, Falanga A, Torri V, Taraboletti G, Giavazzi R, Belotti D. (2018). Soluble stroma-related biomarkers for detecting pancreatic cancer and assessing treatment efficacy. *EMBO Molecular Medicine*, 10(8), 8741.

Appendix II – Measurement of tumor growth and drugs antitumor efficacy evaluation

Tumor volume was estimated according to the formula:

$$TV\ (mm^3) = d^2 * \frac{D}{2}$$

with d=tumor minimum diameter; D=tumor maximum diameter, measured with a Vernier caliper.

The antitumor efficacy of the drugs was measured by tumor volume inhibition (TVI) in treated vs control mice:

$$TVI\ (\%) = 100 - \frac{\text{mean TV treated}}{\text{mean TV control}} * 100$$

Appendix III - List of primary antibodies

Marker (clone)	Supplier (code)	Clonality	Dilution	Application/specificity
Arginase I	Santa Cruz (sc-18354)	Goat polyclonal	1/2000	M2-macrophages
CA9	LS-Bioscience (LS-B273)	Rabbit polyclonal	1/2000	Hypoxic cells
B220 (RA3-6B2)	BD Bioscience (#557390)	Rat monoclonal	1/800	B-lymphocytes
CD3ε	Santa Cruz (sc-1127)	Goat polyclonal	1/2000	T-lymphocytes
CD31 (SZ31)	Dianova (DIA-310)	Rat monoclonal	1/100	Endothelium
Cleaved Caspase-3	Cell signaling (asp175)	Rabbit polyclonal	1/2000	Apoptotic cells
Human MHC I	Abcam (ab52922)	Rabbit polyclonal	1/600	Human cells
Iba1	Wako (#019-19741)	Rabbit polyclonal	1/2000	Mononuclear-phagocytes
iNOS	Abcam (ab15323)	Rabbit polyclonal	1/100	M1-macrophages
Ly6g (1A8)	BD Bioscience (#551459)	Rat monoclonal	1/1000	Neutrophils
MMP-7 (D4H5)	Cell signaling (#3801)	Rabbit monoclonal	1/400	Matrix metalloproteinasis-7
NKp46/NCR1	R&D (AF2225)	Goat polyclonal	1/500	Natural Killer cells
Pimonidazole	Hypoxyprobe (PAb2627AP)	Rabbit polyclonal	1/700	Hypoxic cells (pretreatment with pimonidazole required)
THBS-2	Thermoscientific (PA5-50843)	Rabbit polyclonal	1/50	Thrombospondin-2
TIMP1	R&D (AF980)	Goat polyclonal	1/900	Tissue inhibitor of metalloproteinasis-1

Appendix IV – Immunohistochemistry protocol

Step	Protocol	Time, temperature
Epitope retrieval	Heat induced epitope retrieval (HIER) (Buffer H pH9)	40', 94°C
Endogenous peroxidase inhibition	3% H2O2	10', room temperature (RT)
Aspecific binding blocking	10% normal serum*	30', RT
Primary antibody	Primary antibody (for dilution refer to appendix III)	1h, RT
Secondary antibody	Byotinilated secondary antibody (anti-rabbit / anti-rat / anti-goat; 1:200)	30', RT
Signal amplification	Avidin-biotin-peroxidase complex	30', RT
Development of the immune reaction	3,3'-Diaminobenzidine	5', RT
Counterstain	Mayer's Hematoxylin	2', RT

*normal rabbit serum for primary antibodies raised in goat and rat; normal goat serum for primary antibodies raised in rabbit.

Appendix V – Sirius red stain protocol

REAGENTS

<u>Picro-sirius red Solution</u>

Sirius red F3B	0.5 g
Saturated aqueous solution of picric acid	500 ml

<u>Acidified water</u>

Acetic acid (glacial)	5 ml
Water (tap or distilled)	1 L

PROCEDURE

1. Deparaffinize and rehydrate sections to distilled water
2. Stain in Picro-sirius red solution   1 h
3. Wash in 2 changes of acidified water
4. Physically remove most of the water from the slides by vigorous shaking
5. Rapidly dehydrate in 2 changes of 100% ethanol   15''
   and 30"
6. Clear in xylene   2'
7. Mount with resinous mounting medium

RESULTS

Bright field microscopy

- Collagen...…….…..…………………………………………..……….....red
- Background…………….……………………………...............................yellow

Polarized light

- Large collagen fibers...bright yellow or orange
- Thin collagen fibers...green

The birefringence is highly specific for collagen: a few materials, including type 4 collagen basement membranes, keratohyaline granules and some types of mucus, are stained red but are not birefringent.

Appendix VI – Alcian blue stain protocol

REAGENTS

<u>3% Acetic Acid Solution</u>

Glacial acetic acid	3 ml
Distilled water	100 ml

<u>Alcian blue Solution</u>

3% glacial acetic acid	100 ml
Alcian blue 8GX	1 g

Mix, adjust pH to 2.5 using acetic acid.

<u>Neutral red stain solution</u>

Neutral red (CI 50040)	1 g
Distilled water	100 ml
Glacial acetic acid	0.1 ml

Dissolve the dye in the distilled water. Add the acid and mix well. Filter into the reagent bottle.

PROCEDURE

1. Deparaffinize and rehydrate sections to distilled water
2. Stain in Alcian blue solution   30'
3. Rinse in running tap water   5'
4. Rinse in distilled water
5. Counterstain with neutral red stain   1'
6. Rinse in distilled water
7. Rapidly dehydrate in absolute alcohol   1'
8. Clear in xylene   2' and 5'
9. Mount with resinous mounting medium

RESULTS

- Acid mucins (except some of the strongly sulphated groups)…..................…… blue
- Nuclei……………………………………...… red

Appendix VII – Digital Image Analysis

Digital image analysis (DIA) of histochemical and immunohistochemical stain was performed according to one of the following procedures, depending on the aim of the analysis. In general, for all DIA purposes, digital images from the same experiment were obtained with the same parameters.

Manual count with Image J[1]

AIM. To count repetitive elements. In the studies presented here, manual count was used to assess microvessel density in slides stained by IHC with CD31.

PROCEDURE

1. Open an image
2. Select the "multi-point tool"
3. Click once on each object to be counted. In the point tool window, selected objects will be automatically counted.

Area fraction with Image J[1]

AIM. To measure the percentage of positive-stained area (area fraction).

PROCEDURE

1. Open an image
2. Analyze > set measurements > select "area fraction"
3. Image > color > split channels
4. Select the blue one (for IHC stained slides with DAB chromogen) or the green one (Sirius red stain).
5. Image > adjust > threshold > choose the appropriate value
6. Analyze > measure

The same threshold has to be applied to all the images from the same batch.

Area fraction with Orbit Image Analysis[2]

AIM. To measure the percentage of positive-stained area (area fraction).

PROCEDURE

1. Open an image
2. Set up classes (in classification tab)
3. With the polygon tool, select some regions for each class
4. Train the model
5. Classify
6. Move the slider to check the accuracy of classification
7. If the classification is not accurate enough, repeat passages 3-6.

The same model has to be used to evaluate all the images from the same batch. Note that training the model on different images results in a more accurate classification.

---

[1] Image J: Schneider, C. A., Rasband, W. S., & Eliceiri, K. W. (2012). NIH Image to ImageJ: 25 years of image analysis. Nature methods, 9(7), 671.

[2] Orbit Image Analysis: Stritt, M., Stalder, A. K., & Vezzali, E. (2019). Orbit Image Analysis: An open-source whole slide image analysis tool. bioRxiv [Epub ahed of print].

Acknowledgments